Development of Convective-Scale Static Background Error Covariance within GSI-Based Hybrid EnVar System for Direct Radar Reflectivity Data Assimilation

YONGMING WANG[a] AND XUGUANG WANG[a]

[a] *School of Meteorology, University of Oklahoma, Norman, Oklahoma*

(Manuscript received 1 July 2020, in final form 9 May 2021)

ABSTRACT: A convective-scale static background-error covariance (BEC) matrix is further developed to include the capability of direct reflectivity assimilation and evaluated within the GSI-based three-dimensional variational (3DVar) and hybrid ensemble–variational (EnVar) methods. Specific developments are summarized as follows: 1) Control variables (CVs) are extended to include reflectivity, vertical velocity, and all hydrometeor types. Various horizontal momentum and moisture CV options are included. 2) Cross correlations between all CVs are established. 3) A storm intensity-dependent binning method is adopted to separately calculate static error matrices for clear-air and storms with varying intensities. The resultant static BEC matrices are simultaneously applied at proper locations guided by the observed reflectivity. 4) The EnVar is extended to adaptively incorporate static BECs based on the quality of ensemble covariances. Evaluation and examination of the new static BECs are first performed on the 8 May 2003 Oklahoma City supercell. Detailed diagnostics and 3DVar examinations suggest zonal/meridional winds and pseudo–relative humidity are selected as horizontal momentum and moisture CVs for direct reflectivity assimilation, respectively; inclusion of cross correlations favors spin up and maintains the analyzed storms; application of binning improves characteristics and persistence of the simulated storm. Relative to an experiment using the full ensemble BECs (Exp-PureEnVar), incorporating static BECs in hybrid EnVar reduces spinup time and better analyzes reflectivity distributions while the background ensemble is deficient in sampling errors. Compared to both pure 3DVar and Exp-PureEnVar, hybrid EnVar better predicts reflectivity distributions and better maintains a strong mesocyclone. Further examination through the 20 May 2013 Oklahoma supercells confirms these results and additionally demonstrates the effectiveness of adaptive hybridization.

KEYWORDS: Convective-scale processes; Kalman filters; Variational analysis; Cloud resolving models; Data assimilation; Numerical weather prediction/forecasting

1. Introduction

Accurate initialization of storms is essential to the success of convective-scale numerical weather prediction (NWP). Given the high spatiotemporal resolution capable of depicting the internal structure and evolution of storms (Lilly 1990), radar reflectivity and radial velocity are the most widely used observations (Sun 2005; Dowell et al. 2011) for convective-scale data assimilation (DA). However, the effective assimilation of radar data still poses major challenges, especially the radar reflectivity assimilation in a dynamically and thermodynamically coherent fashion. Several methods have been proposed to assimilate radar observations, including cloud analysis (CA; e.g., Albers et al. 1996; Hu et al. 2006); pure variational assimilation (3DVar/4DVar; e.g., Sun and Crook 1997; Gao and Stensrud 2012; H. Wang et al. 2013a,b); and DA methods involving the use of ensembles such as the ensemble Kalman filter (EnKF; e.g., Dowell et al. 2004, 2011; Johnson et al. 2015) and ensemble–variational (EnVar; e.g., Wang and Wang 2017) methods.

In both a pure variational and a hybrid EnVar approach for convective-scale radar DA, one critical component is the static background-error covariances (BECs) that can reflect the convective-scale error variance and spatial and cross-variable correlation statistics. Such a static BEC matrix is established and widely used for global large-scale pure Var (e.g., Derber and Bouttier 1999; Lorenc et al. 2000; Ingleby 2001) or hybrid EnVar systems (e.g., Buehner 2005; Buehner et al. 2010a,b; Clayton et al. 2013; X. Wang et al. 2013; Buehner et al. 2013). These early studies have demonstrated that the static BECs can compensate the flow-dependent ensemble covariances when they are deficient to sample the background errors due to either the use of limited ensemble members or undersampling of model errors (e.g., X. Wang et al. 2007a,b, 2009; Buehner et al. 2010a,b; Buehner et al. 2013). For convective-scale DA, such deficiency of the ensemble covariance can be even more problematic due to e.g., many sources of model errors. Therefore, efforts are needed to construct a static BEC matrix for convective-scale DA. Several earlier studies (Brousseau et al. 2008; Montmerle and Berre 2010; Michel et al. 2011) have suggested the static BECs appropriate for convective scales favor convective-scale DA and forecasts.

One challenge to specify the static BECs for convective-scale radar DA is the prescription of the cross-variable relationship. All previous pure Var studies typically neglected the cross-correlations between hydrometeors and other variables in their static BECs (Gao and Stensrud 2012; Gao et al. 2004; Johnson et al. 2015; Sun et al. 2016; Liu et al. 2019). Even when vertical velocity was included as the CV, it was treated as a univariate variable in the static BEC matrix without any correlations to other variables (Gao and Stensrud 2012; Gao et al. 2004; Johnson et al. 2015; Liu et al. 2019). Such inconsistencies or lack of updates of other variables in 3DVar can lead to unrealistic duration and structure of storms (Johnson et al. 2015).

Corresponding author: Xuguang Wang, xuguang.wang@ou.edu

DOI: 10.1175/MWR-D-20-0215.1

Another challenge to specify the static BECs for convective-scale radar DA is the appropriate inclusion and selection of control variables (CVs). For momentum CVs, only a limited number of studies include the vertical momentum CV, a critical variable for the nonhydrostatic convective-scale motions, in the static BEC matrix (Gao and Stensrud 2012; Gao et al. 2004; Johnson et al. 2015; Liu et al. 2019). For horizontal momentum CVs, streamfunction ψ and velocity potential χ have been historically and widely used in large-scale variational DA (e.g., Berre 2000; Lorenc et al. 2000; Wu and Purser 2002; Xiao et al. 2005; Huang et al. 2009; H. Wang et al. 2013a,b; X. Wang et al. 2008a,b, 2013), considering the benefit that χ is approximately linearly linked with the mass fields through the geostrophic assumption. However, such benefit is not valid at convective scales (Berre 2000). Several studies have compared the use of zonal/meridional winds (u/v) or vorticity/divergence (ζ/η) relative to ψ/χ as the horizontal momentum CVs (e.g., Xie and MacDonald 2012, Sun et al. 2016). However, these studies were performed either without assimilation of reflectivity (Xie and MacDonald 2012) or with indirect assimilation of reflectivity (Sun et al. 2016). For the moisture CV, several studies highlighted the strong statistical couplings of specific humidity (q) with other variables and used q as the moisture CV in construction of their convective-scale static BECs (e.g., Montmerle and Berre 2010; Michel et al. 2011). However, Dee and Da Silva (2003) found that q as the moisture CV leads to harmful extrapolation errors due to its large vertical gradients and recommended pseudorelative humidity (rh) as the moisture CV to construct the static BEC matrix. Therefore, uncertainty remains to select the moisture CV in the construction of the convective-scale static BECs for direct Var-based reflectivity assimilation.

Recently, Wang and Wang (2017) developed an approach to directly assimilate reflectivity within the Gridpoint Statistical Interpolation (GSI)-based EnVar framework. This EnVar method includes reflectivity as a state variable and therefore bypasses the issue of variational minimization caused by the nonlinear reflectivity observation operator. This approach has been demonstrated to improve the analyses and forecasts for a tornadic supercell storm (Wang and Wang 2017) and systematic convective-scale forecasts over the continental United States (CONUS) (Duda et al. 2019). Given the challenges, unknowns, and limitations of the static BECs in previous Var studies for direct reflectivity assimilation, the primary goals of this study are (i) to construct a convective-scale static BEC matrix appropriate for the direct reflectivity assimilation, (ii) to implement it within the GSI-based 3DVar and EnVar systems that are capable of directly assimilating radar reflectivity observations (Wang and Wang 2017), and (iii) to perform experiments on two supercell events to evaluate the effectiveness of this new static BECs. Briefly, compared to the static BEC models in earlier studies, the newly constructed static BECs (i) includes vertical velocity, reflectivity, and all hydrometeor types as CVs; (ii) permits the cross-correlations between hydrometeors/vertical velocity and other dynamic and thermodynamic variables; (iii) allows building background-error statistics for clear-air and storms with varying intensities, extended from Michel et al. (2011); (iv) selects horizontal momentum and moisture CVs for direct reflectivity assimilation; and (v) can be adaptively hybridized with the ensemble BECs in the hybrid EnVar depending on the quality of the ensemble.

This paper is organized as follows. Section 2 describes the GSI-based hybrid EnVar algorithm, including the methodology of construction and implementation of the convective-scale static BECs for the direct reflectivity assimilation. A description of the 8 May 2003 supercell, datasets used to calculate static BECs, and the experimental designs are presented in section 3. Section 4 first presents the results toward optimizing the static BECs for the direct assimilation of reflectivity through analytical approaches and running pure 3DVar experiments, and then compares the results in hybrid EnVar with and without the static BECs on the analysis and prediction of the 8 May 2003 tornadic supercell storm. Results for another case on 20 May 2013 are also included. Conclusions are given in section 5.

2. Methodology

a. Brief review of GSI-based hybrid EnVar

Wang (2010) described the mathematical framework of the GSI-based hybrid EnVar system, which utilizes a blended BEC matrix including flow-dependent and static BECs. The system is designed to produce a hybrid increment $\mathbf{x}'$ that minimizes the following cost function J:

$$\begin{aligned} J(\mathbf{x}_1', \mathbf{a}) &= \beta_1 J_1 + \beta_2 J_e + J_o \\ &= \beta_1 0.5(\mathbf{x}_1')^{\mathrm{T}} \mathbf{B}_1^{-1}(\mathbf{x}_1') + \beta_2 0.5(\mathbf{a})^{\mathrm{T}} \mathbf{A}^{-1}(\mathbf{a}) \\ &\quad + 0.5\left(\mathbf{y}^{o\prime} - \mathbf{H}\mathbf{x}'\right)^{\mathrm{T}} \mathbf{R}^{-1}\left(\mathbf{y}^{o\prime} - \mathbf{H}\mathbf{x}'\right). \end{aligned} \tag{1}$$

In the term J_1, $\mathbf{B}_1$ represents the static BEC matrix, and its associated analysis increment is $\mathbf{x}_1'$. The term J_e shows the cost function term associated with the ensemble BECs. Here, vector $\mathbf{a}$ is formed by concatenating K vectors $\mathbf{a}_k$, $k = 1, \ldots, K$, denoting the extended CVs for each ensemble member, where K is the ensemble size. The covariance localization for the ensemble BECs is determined in the block-diagonal matrix $\mathbf{A}$. The static and ensemble BECs are weighted by two factors β_1 and β_2, respectively. The two factors are related by $(1/\beta_1) + (1/\beta_2) = 1$. The last term is the observation term J_o, where $\mathbf{R}$ is the observation error covariance, $\mathbf{y}^{o\prime}$ is the innovation vector, and $\mathbf{H}$ is the linearized observation operator. The hybrid increment $\mathbf{x}'$ is defined as

$$\mathbf{x}' = \mathbf{x}_1' + \mathbf{D}\mathbf{a} = (\mathbf{I} \quad \mathbf{D}) \begin{pmatrix} \mathbf{x}_1' \\ \mathbf{a} \end{pmatrix}, \tag{2}$$

where $\mathbf{D}$ is denoted as $[\mathrm{diag}(\mathbf{x}_1^e) \cdots \mathrm{diag}(\mathbf{x}_K^e)]$, $\mathbf{x}_k^e$ is the kth ensemble perturbation divided by $\sqrt{K-1}$, $\mathbf{I}$ is an identity matrix, and the operator diag translates a vector to a diagonal matrix (Wang 2010).

Given the typically large number of grid points used in NWP models, the BEC matrix and its inverse [sizes of $O(10^7 \times 10^7)$] are difficult to be explicitly calculated during minimizing the cost function of Eq. (1). To avoid the large dimensions of the

inverse problem, the minimization procedure in GSI is preconditioned upon the full BEC matrix by defining a new variable (Derber and Rosati 1989; Wang 2010):

$$\mathbf{z} = \mathbf{B}^{-1}\mathbf{x} = \begin{pmatrix} \beta_1\mathbf{B}_1^{-1} & \mathbf{0} \\ \mathbf{0} & \beta_2\mathbf{A}^{-1} \end{pmatrix} \begin{pmatrix} \mathbf{x}_1' \\ \mathbf{a} \end{pmatrix} = \begin{pmatrix} \beta_1\mathbf{B}_1^{-1}\mathbf{x}_1' \\ \beta_2\mathbf{A}^{-1}\mathbf{a} \end{pmatrix}, \quad (3)$$

where $\mathbf{B}$ is

$$\mathbf{B} = \begin{pmatrix} \frac{1}{\beta_1}\mathbf{B}_1 & \mathbf{0} \\ \mathbf{0} & \frac{1}{\beta_2}\mathbf{A} \end{pmatrix}, \quad (4)$$

and $\mathbf{x}$ is the CV for the hybrid system:

$$\mathbf{x} = \begin{pmatrix} \mathbf{x}_1' \\ \mathbf{a} \end{pmatrix}. \quad (5)$$

In practice, $\mathbf{B}$ is modeled to avoid the large dimensions of the explicit calculation problem. Specifically, the same recursive filter transform is applied to approximate the K identically prescribed correlation submatrices in $\mathbf{A}$ (Wang et al. 2008a; Wang 2010). The matrix $\mathbf{B}_1$ is decomposed to several operators:

$$\mathbf{B}_1 = \mathbf{U}_p\mathbf{S}\mathbf{U}_v\mathbf{U}_h\mathbf{U}_h^{\mathrm{T}}\mathbf{U}_v^{\mathrm{T}}\mathbf{S}^{\mathrm{T}}\mathbf{U}_p^{\mathrm{T}}, \quad (6)$$

and each operator accounting for an elemental transform is individually modeled (Barker et al. 2004; Descombes et al. 2015). The physical transform $\mathbf{U}_p$ defines the set of CVs associated with $\mathbf{B}_1$ and their cross-variable correlations. The matrices $\mathbf{U}_h$ and $\mathbf{U}_v$ are horizontal and vertical transforms, respectively, defining the horizontal and vertical autocorrelations for the CVs. Both $\mathbf{U}_h$ and $\mathbf{U}_v$ transforms are modeled through the recursive filters (Hayden and Purser 1995; Purser et al. 2003a,b) in GSI for the regional applications. The diagonal matrix $\mathbf{S}$ consists of the standard deviations of the background errors of the CVs. More details on these operators and their specific calculations can be found in Descombes et al. (2015).

b. *Development of convective-scale static background-error covariance for direct reflectivity assimilation*

This section provides the specific developments of the convective-scale static BEC matrix introduced in section 1.

1) AUGMENTING CONTROL VARIABLES ASSOCIATED WITH REFLECTIVITY AND CONSTRUCTING THEIR CROSS-VARIABLE CORRELATIONS

To construct $\mathbf{B}_1$ for direct reflectivity assimilation at convective scales, we first augment CVs to include reflectivity, all hydrometeor types, and vertical velocity. To effectively spread observation information, $\mathbf{B}_1$ is expected not only to depict horizontal and vertical spatial structures of covariance, but also to include the cross-variable correlations (Daley 1991). Background errors of hydrometers are highly correlated with errors in other variables (Michel et al. 2011). However, as discussed in section 1, the covariance between hydrometeors and other CVs were often ignored in the previous Var-based reflectivity assimilation (e.g., Caya et al. 2005; Carley 2012; H. Wang et al. 2013a; Johnson et al. 2015) and in the current GSI. A proper cross-variable correction is expected to minimize adjustment and spinup at the beginning of a forecast (Sun et al. 2016) through projecting increments from radar observations and related variables to other variables during the DA procedure. Therefore, in addition to extending the CVs, their cross-variable correlations are augmented. Equation (7) shows the extended CVs and their cross-variable correlations, i.e., the $\mathbf{U}_p$ transform:

$$\begin{pmatrix} u \\ v \\ t \\ \mathrm{ps} \\ \mathrm{rh} \\ w \\ \mathrm{ql} \\ \mathrm{qr} \\ \mathrm{qs} \\ \mathrm{qi} \\ \mathrm{qg} \\ \mathrm{dbz} \end{pmatrix} = \begin{pmatrix} \mathbf{I} & 0 & 0 & 0 & 0 & 0 & 0 & 0 & 0 & 0 & 0 & 0 \\ \mathbf{r}_{11} & \mathbf{I} & 0 & 0 & 0 & 0 & 0 & 0 & 0 & 0 & 0 & 0 \\ \mathbf{r}_{21} & \mathbf{r}_{22} & \mathbf{I} & 0 & 0 & 0 & 0 & 0 & 0 & 0 & 0 & 0 \\ \mathbf{r}_{31} & \mathbf{r}_{32} & \mathbf{r}_{33} & \mathbf{I} & 0 & 0 & 0 & 0 & 0 & 0 & 0 & 0 \\ \mathbf{r}_{41} & \mathbf{r}_{42} & \mathbf{r}_{43} & \mathbf{r}_{44} & \mathbf{I} & 0 & 0 & 0 & 0 & 0 & 0 & 0 \\ \mathbf{r}_{51} & \mathbf{r}_{52} & \mathbf{r}_{53} & \mathbf{r}_{54} & \mathbf{r}_{55} & \mathbf{I} & 0 & 0 & 0 & 0 & 0 & 0 \\ \mathbf{r}_{61} & \mathbf{r}_{62} & \mathbf{r}_{63} & \mathbf{r}_{64} & \mathbf{r}_{65} & \mathbf{r}_{66} & \mathbf{I} & 0 & 0 & 0 & 0 & 0 \\ \mathbf{r}_{71} & \mathbf{r}_{72} & \mathbf{r}_{73} & \mathbf{r}_{74} & \mathbf{r}_{75} & \mathbf{r}_{76} & \mathbf{r}_{77} & \mathbf{I} & 0 & 0 & 0 & 0 \\ \mathbf{r}_{81} & \mathbf{r}_{82} & \mathbf{r}_{83} & \mathbf{r}_{84} & \mathbf{r}_{85} & \mathbf{r}_{86} & \mathbf{r}_{87} & \mathbf{r}_{88} & \mathbf{I} & 0 & 0 & 0 \\ \mathbf{r}_{91} & \mathbf{r}_{92} & \mathbf{r}_{93} & \mathbf{r}_{94} & \mathbf{r}_{95} & \mathbf{r}_{96} & \mathbf{r}_{97} & \mathbf{r}_{98} & \mathbf{r}_{99} & \mathbf{I} & 0 & 0 \\ \mathbf{r}_{101} & \mathbf{r}_{102} & \mathbf{r}_{103} & \mathbf{r}_{104} & \mathbf{r}_{105} & \mathbf{r}_{106} & \mathbf{r}_{107} & \mathbf{r}_{108} & \mathbf{r}_{109} & \mathbf{r}_{1010} & \mathbf{I} & 0 \\ \mathbf{r}_{111} & \mathbf{r}_{112} & \mathbf{r}_{113} & \mathbf{r}_{114} & \mathbf{r}_{115} & \mathbf{r}_{116} & \mathbf{r}_{117} & \mathbf{r}_{118} & \mathbf{r}_{119} & \mathbf{r}_{1110} & \mathbf{r}_{1111} & \mathbf{I} \end{pmatrix} \begin{pmatrix} u \\ v_u \\ t_u \\ \mathrm{ps}_u \\ \mathrm{rh}_u \\ w_u \\ \mathrm{ql}_u \\ \mathrm{qr}_u \\ \mathrm{qs}_u \\ \mathrm{qi}_u \\ \mathrm{qg}_u \\ \mathrm{dbz}_u \end{pmatrix}. \quad (7)$$

The matrix that premultiplies the right most column of Eq. (7) is called physical transform or multivariate balance operator. The rightmost column of Eq. (7) comprises CVs, which include the zonal wind (u), unbalanced meridional wind (v_u), unbalanced temperature (t_u), unbalanced surface pressure (ps_u), and unbalanced pseudorelative humidity (rh_u), typically used in Var (e.g., Zou et al. 1995; Sun et al. 1991; Sun and Crook 1997; Gao et al. 1999; Sun et al. 2016). To achieve the goal of direct reflectivity assimilation without the tangent linear and adjoint of nonlinear reflectivity operator, the CV is first extended to include the unbalanced reflectivity (dbz_u). Consistent with the previous studies (e.g., Gao and Stensrud 2012; Johnson et al. 2015; Wang and Wang 2017), as the vertical velocity is used in the radial velocity operator and updraft is a vital dynamical variable for convective scales, the unbalanced vertical velocity (w_u) is added as a CV. Consistent with the previous Var-based

reflectivity assimilation (e.g., Caya et al. 2005; Carley 2012; H. Wang et al. 2013a; Johnson et al. 2015), the unbalanced mixing ratios of hydrometer [cloud water (ql_u), rainwater (qr_u), snow (qs_u), cloud ice (qi_u), and graupel (qg_u)] are also included in this study. The subscript "u" as well as the word "unbalanced" refer to the residual after a statistical balance with the preceding CVs is removed from the full model variable. For example, t_u is calculated by subtracting its balanced part attributed to u and v_u from the full temperature (t) perturbation following

$$t_u = t - \mathbf{r}_{21}u - \mathbf{r}_{22}v_u. \tag{8}$$

Here the balance operator $\mathbf{r}_{ij}$, where $i = 1, \ldots, 11$, and $j = 1, \ldots, 11$, represents the linear regression to model the multivariate error covariances. Following a similar procedure, these unbalanced fields in Eq. (7) are successively calculated. The correlation among CVs can be shown to be zero, a desirable feature for an effective solution of the conditioning issue (Michel et al. 2011). The multivariate covariance is expected to allow the state variables to be updated more coherently. The reader can refer to Michel et al. (2011) and Descombes et al. (2015) for the detailed calculations of the balance operators.

To identify the optimal horizontal momentum and moisture CVs for the direct reflectivity assimilation, this study includes two additional horizontal momentum CV choices using ψ/χ_u (CV_$\psi\chi$) and ζ/η_u (CV_$\zeta\eta$), as well as one additional moisture CV option using q_u (CV_q). These will be compared with the other corresponding CV options (CV_uv and CV_rh) used in Eq. (7).

2) The storm intensity-dependent binning

Previous studies found that significant differences in the background-error statistics exist between precipitating and nonprecipitating areas (Caron and Fillion 2010; Montmerle and Berrer 2010; Michel et al. 2011). Therefore, homogeneous background-error statistics are inappropriate to concurrently account for both storms and clear-air locations. To increase the heterogeneity of static BECs, this study simultaneously applies different static error statistics at appropriate locations based on a geographical mask as in Michel et al. (2011) and Ménétrier and Montmerle (2011). The binary geographical mask partitions the entire domain into three bins featured by different storm intensities. The storm intensity here is represented by composite reflectivity. Specifically, the bins of the "strong storm" $\mathbf{P}_s$ and the "clear-air" $\mathbf{N}$ represent the points where the composite reflectivity in both ensemble-mean and all background ensemble members are greater than 35 dBZ and weaker than 10 dBZ, respectively; the areas with the composite reflectivity between 10 and 35 dBZ in both ensemble-mean and each forecast member compose the bin of "weak storm" $\mathbf{P}_w$. Locations where the ensemble-mean and each forecast member do not fall in the same category are omitted from the static BEC computation. In this study, the grid points in $\mathbf{P}_s$ take ~34% of the storm area (the composite reflectivity above 10 dBZ); the remaining 66% consists of the grid points in $\mathbf{P}_w$; the number of grid points in $\mathbf{N}$ is ~20 times of that in the storm area. Further optimizing these reflectivity thresholds to distinguish the above bins may be needed in future work. To calculate the static BEC matrix, each operator in Eq. (6) is spatially averaged over each bin. Then the decomposed $\mathbf{B}_1$ of Eq. (6) is modified to Eq. (9) as in Michel et al. (2011):

$$\begin{aligned}\mathbf{B}_1 = {} & \mathbf{P}_s\mathbf{U}_p^s\mathbf{S}^s\mathbf{U}_v^s\mathbf{U}_h^s(\mathbf{U}_p^s\mathbf{S}^s\mathbf{U}_v^s\mathbf{U}_h^s)^{\mathrm{T}}\mathbf{P}_s^{\mathrm{T}} \\ & + \mathbf{P}_w\mathbf{U}_p^w\mathbf{S}^w\mathbf{U}_v^w\mathbf{U}_h^w(\mathbf{U}_p^w\mathbf{S}^w\mathbf{U}_v^w\mathbf{U}_h^w)^{\mathrm{T}}\mathbf{P}_w^{\mathrm{T}} \\ & + \mathbf{N}\mathbf{U}_p^N\mathbf{S}^N\mathbf{U}_v^N\mathbf{U}_h^N(\mathbf{U}_p^N\mathbf{S}^N\mathbf{U}_v^N\mathbf{U}_h^N)^{\mathrm{T}}\mathbf{N}^{\mathrm{T}}. \end{aligned} \tag{9}$$

During the Var update, the storm intensities provided by the reflectivity observations are employed to define the geographical mask to guide on where a particular class of $\mathbf{B}_1$ is adopted. For example, the BEC matrices from the bin of $\mathbf{P}_s$, $\mathbf{N}$, and $\mathbf{P}_w$ are, respectively, applied on the locations where the observed reflectivity exceeding 35 dBZ, less than 10 dBZ, and between 10 and 35 dBZ. To a certain extent, such binning method allows the static BECs to be partially flow dependent.

c. *The formulation of adaptively incorporating convective-scale background-error covariance in GSI-based hybrid EnVar*

One goal of incorporating static BECs in hybrid EnVar is to mitigate the deficiency of the ensemble in sampling the background errors. Conversely, when the ensemble has a sufficiently good quality, the full ensemble BECs are used. To make sure that the static BECs are properly blended with the ensemble BECs, a consistency ratio (CR) is used as an indicator of ensemble quality to define the regions where the combination of static and ensemble BECs is required. Similar to Dowell and Wicker (2009), the CR here denotes as the ratio of the total spread (including observation error variance and ensemble variance) over the square root of the averaged squared innovation (observation-minus-background) for reflectivity. After projecting the computed CR into the model space using a bilinear interpolation, a spatial mask is then defined by vector $\mathbf{m}$ whose components are composed of $1/\beta_1$ and 0 for the areas where CR $< \alpha$ and CR $\geq \alpha$, respectively, where $0 < \alpha \leq 1$. The scalar β_1 is the same as that used in Eq. (1) to indicate the weight placed on the static BEC matrix. Vector $\mathbf{m}$ has a length n that represents the number of state variables. The value of $1/\beta_1$ can be varied based on the CR value following a similar approach for the estimation of the inflation factors in Minamide and Zhang (2019). In this study, the static BEC matrix with a fixed covariance weight is only applied on the areas with CR $<$ α, where the ensemble spread is insufficient. Otherwise, the full ensemble covariances are applied where the sufficient spread is indicated by CR $\geq \alpha$. For the observed clear-air areas, the value of CR is forced to be 1. In other words, the full ensemble covariances are applied in both clear-air and storm areas with CR $\geq \alpha$. The hybridized BECs are used in storm areas with CR $< \alpha$, α is a tunable parameter. In this study, $\alpha = 1.0$ is used.

Mathematically, the resultant $\mathbf{B}$ matrix in Eq. (4) becomes

$$\mathbf{B} = \begin{bmatrix} \mathbf{M}_1^{-1/2}\mathbf{B}_1\mathbf{M}_1^{-1/2^{\mathrm{T}}} & \mathbf{0} \\ \mathbf{0} & \mathbf{M}_2^{-1/2}\mathbf{A}\mathbf{M}_2^{-1/2^{\mathrm{T}}} \end{bmatrix}. \tag{10}$$

Here the complementary matrices $\mathbf{M}_1 = \mathrm{diag}[\mathbf{m}]$ and $\mathbf{M}_2 = \mathrm{diag}[\mathbf{I} - \mathbf{m}]$ define the spatially adaptive covariance weights, and $\mathbf{I}$ is

the n-dimensional identity vector. The hybrid cost function [Eq. (1)] is accordingly modified to

$$J(\mathbf{x}_1', \mathbf{a}) = 0.5(\mathbf{x}_1')^{\mathrm{T}}(\mathbf{M}_1^{1/2^{\mathrm{T}}}\mathbf{B}_1^{-1}\mathbf{M}_1^{1/2})(\mathbf{x}_1') + 0.5(\mathbf{a})^{\mathrm{T}}(\mathbf{M}_2^{1/2^{\mathrm{T}}}\mathbf{A}^{-1}\mathbf{M}_2^{1/2})(\mathbf{a}) + 0.5\left(\mathbf{y}^{o\prime} - \mathbf{H}\mathbf{x}'\right)^{\mathrm{T}}\mathbf{R}^{-1}\left(\mathbf{y}^{o\prime} - \mathbf{H}\mathbf{x}'\right). \quad (11)$$

Equation (11) is mathematically equivalent to Eq. (1) if $\mathbf{m}$ becomes an identity vector multiplied by the scalar $1/\beta_1$. It can be demonstrated that the minimization of Eq. (11) with respect to adaptive covariance weights can be achieved through the full BEC preconditioning as in the original GSI-based hybrid EnVar minimization (Wang 2010).

3. Experimental design

a. Case overview

We first demonstrate and test the newly proposed method using the 8 May 2003 supercell case. The synoptic-scale environment within Oklahoma on 8 May 2003 promoted a significant outbreak of severe storms by midafternoon (Romine et al. 2008). A relatively deep southerly flow carrying warm and moist air sustained over Texas and Oklahoma all day. A dryline was located in west-central Oklahoma along with the midlevel west-southwesterly flow by 1800 UTC 8 May. Strong vertical wind shear was in place throughout the warm sector. The isolated Oklahoma City (OKC) supercell storm appeared at ~2100 UTC and propagated until 2300 UTC, when it began to weaken and finally dissipate by 0020 UTC 9 May. More details about the evolution of the OKC thunderstorm were introduced in Hu and Xue (2007) and Romine et al. (2008).

Additional results are presented for the 20 May 2013 case in section 4e(3). During 1830–2100 UTC 20 May 2013, three supercell storms initiated and propagated northeastward over central Oklahoma.

b. Calculation and datasets of static background-error covariance

An ensemble method (Fisher 2003) is used to generate the static BEC matrix in this study. The utility GEN_BE_v2.0 described in Descombes et al. (2015) is extended to calculate each operator in Eq. (6) to model the static BECs. Specifically, the static BEC matrix is calculated from the covariances of past ensemble perturbations. The datasets used to calculate the ensemble perturbations are from independent ensemble forecasts at 3-km grid spacing from the OU MAP ensembles[1] of the 2019 National Oceanic and Atmospheric Administration (NOAA) Hazardous Weather Test bed (HWT) Spring Forecast Experiment (Clark et al. 2020). The ensemble forecast is selected when its ensemble mean can well depict the typical structure of a mature supercell storm. Given the computational cost, three supercell storms cases are selected: the supercell storms over northwestern Texas at 2300 UTC 5 May and 0100 UTC 24 May, and over southwestern Oklahoma at 0000 UTC 23 May 2019. For each case, 40-member ensemble perturbations were computed by subtracting the ensemble mean from their ensemble forecasts, yielding 120 members in total to calculate the static BEC matrix.

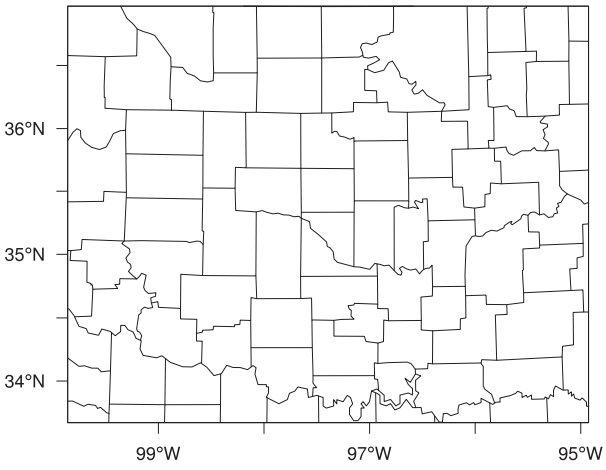

FIG. 1. The domain for storm-scale data assimilation and free forecast.

c. Design of data assimilation and forecast experiments

In this study, many of the DA configurations are designed following Wang and Wang (2017). Briefly, the model uses a single domain (Fig. 1) at a 2-km grid spacing with 226 × 181 horizontal grid points and 50 vertical levels. Only radar reflectivity and radial velocity collected from the WSR-88D radar station KTLX (Oklahoma City, Oklahoma) are assimilated in this domain. The initial conditions (ICs) for the 45-member ensemble as well as their corresponding lateral boundary conditions (LBCs) are interpolated from the 45-member mesoscale ensemble at an 18-km grid spacing in Yussouf et al. (2013). The mean of the mesoscale ensemble provides the ICs and LBCs for the hybrid control member. The reader can refer to Yussouf et al. (2013) and Wang and Wang (2017, 2020) for more details of the mesoscale ensemble. According to earlier studies, the static BEC benefits the hybrid DA system more when the ensemble size is reduced (e.g., X. Wang et al. 2007a, 2009). This result was recently confirmed by Gao and Stensrud (2014) and Kong et al. (2018) for radar DA. The rest of the paper will focus on using the 45-member ensemble.

The Advanced Research Weather Research and Forecasting Model (WRF-ARW) version 3.9.1.1 is employed for all simulations. The model physics configuration is listed in Table 1.

The radar reflectivity and radial velocity observations are retrieved from the National Climatic Data Center (NCDC) archive. The data quality is controlled by the Warning Decision Support System-Integrated Information (WDSSII; Lakshmanan et al. 2007) utility. The observed reflectivity below 5 dBZ, considered as the "no-precipitation" observation, is reset to 0 dBZ to suppress spurious reflectivity in DA (Yussouf et al. 2013; Wang and Wang 2017; Duda et al. 2019). The observation errors

[1] More details about the OU MAP ensembles in the 2019 NOAA HWT can be found in https://hwt.nssl.noaa.gov/sfe/2019/docs/HWT_SFE2019_operations_plan.pdf.

TABLE 1. Model physics configuration.

Physics option	Specification
Microphysics scheme	Thompson scheme (Thompson et al. 2008)
Boundary layer scheme	Mellor–Yamada–Janjić scheme (Mellor and Yamada 1982; Janjić 1990, 1994, 2002)
Land surface model	Noah (Chen and Dudhia 2001)
Longwave–shortwave radiation schemes	RRTMG scheme (Iacono et al. 2008)

for reflectivity and radial velocity are defined as 5 dBZ and 2 m s^{-1}, respectively, consistent with the previous storm-scale DA studies (Dowell et al. 2004; Yussouf et al. 2013; Johnson et al. 2015; Wang and Wang 2017; Duda et al. 2019).

The effectiveness of the static BEC matrix to mitigate the ensemble deficiency is explored in a two-way coupled GSI-based hybrid EnVar (X. Wang et al. 2013). The procedure of DA and forecast configuration is shown in Fig. 2. Starting at 2100 UTC 8 May 2003, both reflectivity and radial velocity observations are assimilated every 15 min for a 1-h period until 2200 UTC. The static BEC matrices are applied at all DA cycles. At each cycle, the two geographical masks for the observation based binning (section 2b) and for the CR-value based adaptive hybridization (section 2c) are computed, respectively. After the DA cycling, a deterministic forecast is then initialized to advance the control analysis from 2200 to 2300 UTC. The control analysis is generated in the hybrid EnVar system leveraging BECs that combine the ensemble BECs with the static BECs. The ensemble square root filter algorithm (EnSRF; Whitaker and Hamill 2002) is utilized to update the ensemble perturbations through assimilating the same radar observations every 15 min. To obtain the final analysis, the analysis ensemble is further recentered around the control analysis. Similar to Wang and Wang (2017), equivalent localization cutoff distances with lengths of 12 km in the horizontal and of 1.1 scale height in the vertical are used in hybrid EnVar and EnSRF. The analysis perturbations are inflated to be 90% of the prior ensemble spread using the relaxation-to-prior-spread inflation method (Whitaker and Hamill 2012).

Given that the static BECs can be directly evaluated in 3DVar without the influences from the ensemble covariances, a series of 3DVar experiments utilizing only the static BECs are first conducted (Table 2) to examine the impact of binning and selection of CVs for the static BECs. The same configuration of storm-scale DA and forecast as in Fig. 2 is adopted in these 3DVar experiments (without the use of ensembles). The benchmark experiment REF uses CV_uv and CV_rh as the horizontal momentum and moisture CVs, respectively, without the use of the binning. Experiments Exp-$\psi\chi$, and Exp-$\zeta\eta$ determine the optimal choice of horizontal momentum CVs when compared against REF using CV_uv. The comparison between REF and Exp-q reveals the influences of different moisture CVs (CV_rh versus CV_q, respectively). Exp-Bin uses the same CVs as REF but incorporates the binning method to evaluate its impact. The static BEC matrix in Exp-Bin is obtained by calculating error statistics for $\mathbf{P}_s$, $\mathbf{N}$, and $\mathbf{P}_w$ bins, respectively.

To explore the impact of including the new static BECs within the hybrid EnVar on the convective-scale analyses and forecasts, two experiments that blend static BECs from Exp-Bin with ensemble covariances, Exp-hyb0.1 and Exp-hyb0.3, are compared to an experiment using the full ensemble covariances, Exp-PureEnVar (Table 3). These hybrid experiments differ by the blending weight on static BECs used for each (10% and 30% for Exp-hyb0.1 and Exp-hyb0.3, respectively).

4. Results

a. *Evaluation of CV selection for the construction of convective-scale static background-error covariance for direct reflectivity assimilation*

1) CHOICE OF HORIZONTAL MOMENTUM CONTROL VARIABLES

Different from the previous studies (e.g., Xie and MacDonald 2012; Sun et al. 2016), this paper examines the selection of horizontal momentum CVs in the context of direct reflectivity

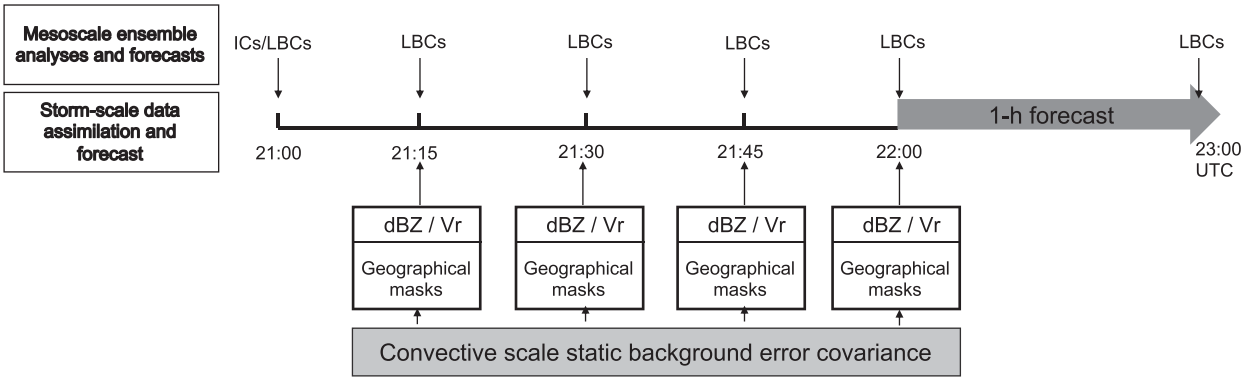

FIG. 2. Schematics of data assimilation experiments with the use of convective-scale static background error covariances. The radar data, including both reflectivity dBZ and radial velocity Vr, are assimilated every 15 min from 2115 to 2200 UTC, with the initial conditions (ICs) and lateral boundary conditions (LBCs) provided by the mesoscale ensemble analyses and forecasts. During the 1-h data assimilation period, the same static background error covariance matrix is used for all cycles, while two varied geographical masks, respectively, for the storm intensity-dependent binning and the adaptive hybridization are defined and used at each cycle. The 1-h forecast is then launched to advance the analysis at 2200 UTC.

TABLE 2. List of 3DVar experiments and their main configurations to construct static error covariance.

Expt	Configurations		
	Momentum CVs	Humidity CV	Use of binning method
REF	u, v_u	rh_u	No
Exp-$\zeta\eta$	ζ, η_u	rh_u	No
Exp-$\psi\chi$	ψ, χ_u	rh_u	No
Exp-q	u, v_u	q_u	No
Exp-Bin	u, v_u	rh_u	Yes

TABLE 3. List of hybrid-EnVar experiments.

Expt	Configurations
Exp-PureEnVar	Background error covariance is fully provided by ensemble covariance
Exp-hyb0.1	Background error covariance comprises 0.1/0.9 weights between static and ensemble covariances
Exp-hyb0.3	Background error covariance comprises 0.3/0.7 weights between static and ensemble covariances

data assimilation. In addition, unlike Sun et al. (2016) only focusing on the comparison between CV_uv and CV_$\psi\chi$, this study compares three horizontal momentum CV choices for convective-scale DA.

To select appropriate horizontal momentum CVs for convective scales, correlations are calculated of various horizontal momentum variables with variables important to convective scales. As a representative example, the vertical cross-variable correlations of w with each of χ, η, and u are shown in Fig. 3. Such correlations are constructed by computing the correlations between each level of w and other variables at every level. The variable χ has the weakest correlation with w across all vertical levels, with maxima less than 0.2 (Fig. 3a). In contrast, the correlation of w with η is largest, where the maximum value is 0.9 (Fig. 3b), presumably governed by the continuity equation. The variable u is moderately correlated with w below the 35th model level with the largest correlation value greater than 0.2 (Fig. 3c). Therefore, CV_uv and CV_$\zeta\eta$ better describe the coupling between w and horizontal momentum variables, relative to CV_$\psi\chi$.

Significant discrepancies in the cost function gradients among different CVs prevent efficient convergence during the variational minimization procedure (Sun and Crook 1997; Wang and Wang 2017). The impact of using various CV choices on the cost function gradient is revealed using the first guess and radar observations valid at 2115 UTC 8 May 2003 from the 3DVar experiments. The J_o gradient with respect to $\mathbf{B}_1^{-1}\mathbf{x}_1'$ is given by

$$\nabla_{\mathbf{B}_1^{-1}\mathbf{x}_1'} J_o = \mathbf{B}_1\mathbf{H}^{\mathrm{T}}\mathbf{R}^{-1}\left(\mathbf{H}\mathbf{x}_1' - \mathbf{y}^{o'}\right). \tag{13}$$

The observation error standard deviations of 5 dBZ and 2 m s^{-1} are assigned to reflectivity and radial velocity, respectively, in $\mathbf{R}$. The summed J_o gradient with respect to horizontal momentum CVs, moisture CV, w_u, and dbz_u from the assimilation of both reflectivity and radial velocity are shown in Fig. 4.

Figures 4a–4c shows the gradient of J_o with respect to three choices of horizontal momentum CVs. Here we compare the J_o gradients with representative variables. In CV_$\psi\chi$ (Fig. 4a), the summed gradient of J_o with respect to ψ has a value greater than 2.1×10^9 that is remarkably larger than that for dbz_u, $\sim 1.1 \times 10^5$. Conversely, the J_o gradient in CV_$\zeta\eta$ has a much larger value for dbz_u (5.9×10^4) than that for ζ (2.2×10^{-2}). In comparison, CV_uv has comparable J_o gradient values with respect to u and dbz_u. This type of ill-conditioned J_o gradient among CVs in CV_$\psi\chi$ and CV_$\zeta\eta$ prevent efficient minimization convergence, as discussed in Sun and Crook (1997) and Wang and Wang (2017). In particular, relative to CV_uv, using CV_$\psi\chi$ has a slower convergence rate during the minimization; with the use of CV_$\zeta\eta$, the minimization fails to converge.

The impact of three choices of horizontal momentum CVs on the locations and characteristics of the 8 May 2003 supercell storm is explored in Fig. 5. The analyzed reflectivity in the forward-flank region from three experiments [Figs. 5a(1),b(1),d(1)] are similar to the size and shape of observations [Fig. 5o(1)]. Exp-$\psi\chi$ and REF reproduce the hook-echo structure at approximately the correct location, as well as the strong low-level rotation, which compare well with the observations. However, Exp-$\zeta\eta$ fails to analyze the hook-echo structure and produces a weak rotation ~10 km ahead of the correct location [Fig. 5b(1)]. In the subsequent forecast, the predicted storm in REF maintains its hook-echo structure, flanks, and strong low-level rotation until 2230 UTC [Figs. 5d(2)–d(4)], which compare well with the observations [Figs. 5o(2)–o(4)]. Conversely, the low-level rotation in Exp-$\psi\chi$ quickly weakens and decays after 2220 UTC and its forward flanks separate into several patches from 2220 UTC trailing some developing spurious cells [Fig. 5a(3)]. Exp-$\zeta\eta$ seems to outperform both Exp-$\psi\chi$ and REF in the size and shape of the predicted reflectivity before 2240 UTC [Figs. 5b(2)–b(5)]. However, its strong low-level rotation propagates from the weak rotation in Fig. 5b(1). This explains the storm in Exp-$\zeta\eta$ moves ~10 km faster than the radar observations and REF during 2210–2240 UTC [Figs. 5b(2)–b(5)].

2) CHOICE OF MOISTURE CONTROL VARIABLE

Figures 6a and 6b show vertical cross-variable correlations between reflectivity (dbz) and moisture variables (rh and q, respectively) over the entire domain. Both moisture variables are similarly correlated to dbz with their maxima coefficients above 0.5. Therefore, options CV_rh and CV_q similarly describe the coupling between reflectivity and moisture variables.

For the J_o gradient, the summed J_o gradient in CV_q with respect to dbz_u has a value 2.2×10^7, which is much greater than that with respect to u ($\sim 4.97 \times 10^4$; Fig. 4d). Therefore, CV_q experiences a much slower convergence rate, relative to CV_rh.

The performance of two moisture CV choices is further examined through comparing REF with Exp-q. Both experiments produce similar reflectivity analyses in terms of

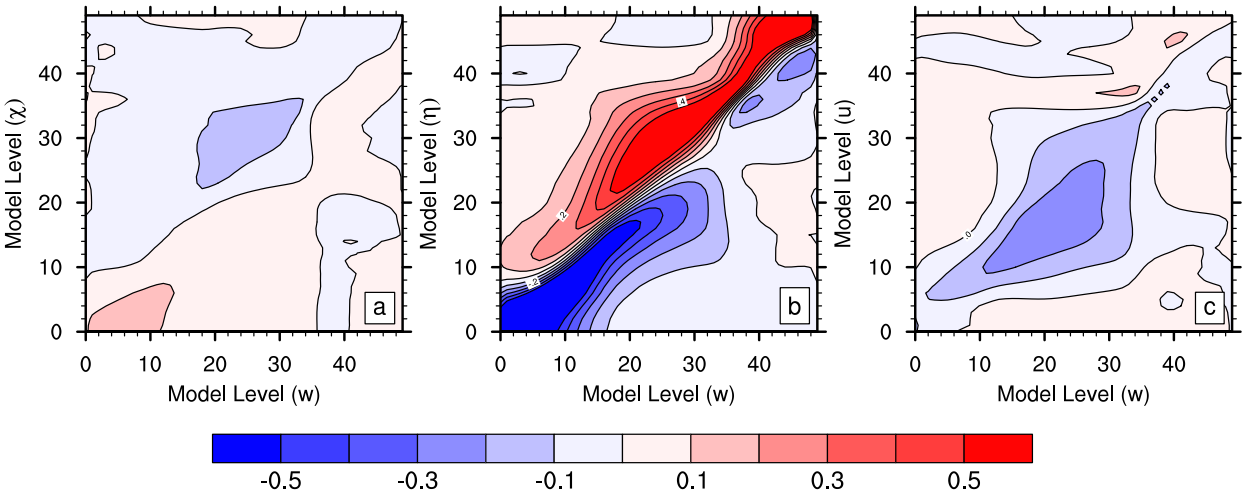

FIG. 3. Vertical cross-variable correlations (a) between vertical velocity w and velocity potential χ, (b) between vertical velocity w and divergence η, and (c) between vertical velocity w and zonal wind u.

hook-echo structure, the forward flank, and the strong low-level rotations [Fig. 5c(1)]. However, Exp-q produces many strong spurious patches in the flanks with multiple rotation centers during 2210–2250 UTC [Figs. 5c(2)–c(5)], which does not compare well with observations.

To conclude, for the 8 May 2003 case, CV_uv and CV_rh are identified as the best horizontal momentum and moisture CVs for convective-scale direct reflectivity assimilation, consistent with the previous studies, e.g., Sun et al. (2016) for horizontal momentum CVs and Dee and Da Silva (2003) for moisture CV.

b. *Descriptions of the newly constructed static BECs and their effects in physical space*

To assess the multivariate relationships in the newly constructed static BECs, the ratios of explained-variance to the total variance are computed through, for example,

$$\text{Ratio} = \frac{(\mathbf{r}_{115}\mathbf{Q}_u)^{\mathrm{T}}\mathbf{Q}_{\mathrm{dbz}}}{\mathbf{Q}_{\mathrm{dbz}}^{\mathrm{T}}\mathbf{Q}_{\mathrm{dbz}}}, \tag{14}$$

where Ratio is the ratio of the dbz variance explained by rh_u, $\mathbf{r}_{115}$ represents the balance operator statistically coupling dbz with rh in Eq. (7), $\mathbf{Q}_u$ and $\mathbf{Q}_{\mathrm{dbz}}$ denote vectors of samples of rh_u and dbz, respectively. The static BECs here use CV_uv and CV_rh as the horizontal momentum and moisture CVs, respectively. Figures 7a and 7b show Ratio for qg and dbz as examples. The variance of qg is primarily contributed by qr_u, rh_u, w_u, qs_u, and qi_u. Below the 20th model level, ~10%–60% of the qg variance is explained, while the explained qg variance above the 20th level exceeds 80%. The large contributions from qr_u, qs_u, and qi_u highlights microphysical process: the increase of low-level rainwater due to the melting of sediment graupel, and the depositional growth and conversion of ice and snow leading to the variations of graupel. The contribution from w_u above the 18th level (~20%) indicates that the formation and enhancement of graupel are largely supported by the strong updraft and the decrease of graupel and its particle falling are associated with the downdraft. The contribution from rh_u peaks at about the midtroposphere, probably indicating the sublimation processes at these levels.

For reflectivity (Fig. 7b), the ratio of the total explained variance relative to the total variance for reflectivity is 41%–85%. The predominant coupling is with qr_u and t_u below the 10th level and with rh_u and qs_u above that. The small contribution from qg could be caused by the fact that variances in both dbz and qg are greatly explained by rh_u, qr_u, and qs_u (Figs. 7a,b). This indicates that a strong coupling exists between dbz and the balanced part of qg at most levels. Furthermore, the coupling between dbz and w is expected to be strong, as the variations of hydrometeors could be directly linked to the vertical motion. The small Ratio by w_u could be due to that dbz strongly correlates with the balanced w, suggested by variances in both w (not shown) and dbz (Fig. 7b) greatly explained by the unbalanced hydrometeors and rh_u. Around 10% of the variance of dbz is explained by t_u, a result reflecting the effect of evaporation and condensation in the cloud at upper levels and in the cold pool near the ground. Figures 7a and 7b also show weak couplings of graupel and reflectivity with u and v_u (Ratio < 3%) across all levels for both variables, suggesting that the variation of hydrometeors has small impact on the changes in horizontal winds.

The vertical mixing is reflected by the structure of vertical correlations. For reflectivity, broad vertical correlations (Fig. 7c) appear at all levels below the 35th level, ~200 hPa. The broad correlations are the consequence of rain falling freely under the 10th level and the variations of hydrometeors associated with the vertical motions in the midtroposphere. Figure 7d shows that the horizontal scales for hydrometeors reach about 6 km, which is smaller than for temperature and other variables (not shown), consistent with Michel et al. (2011). For hydrometeors, the error distributions are physically reasonable. Errors in rainwater tend to be correlated in horizontal only below the 10th level,

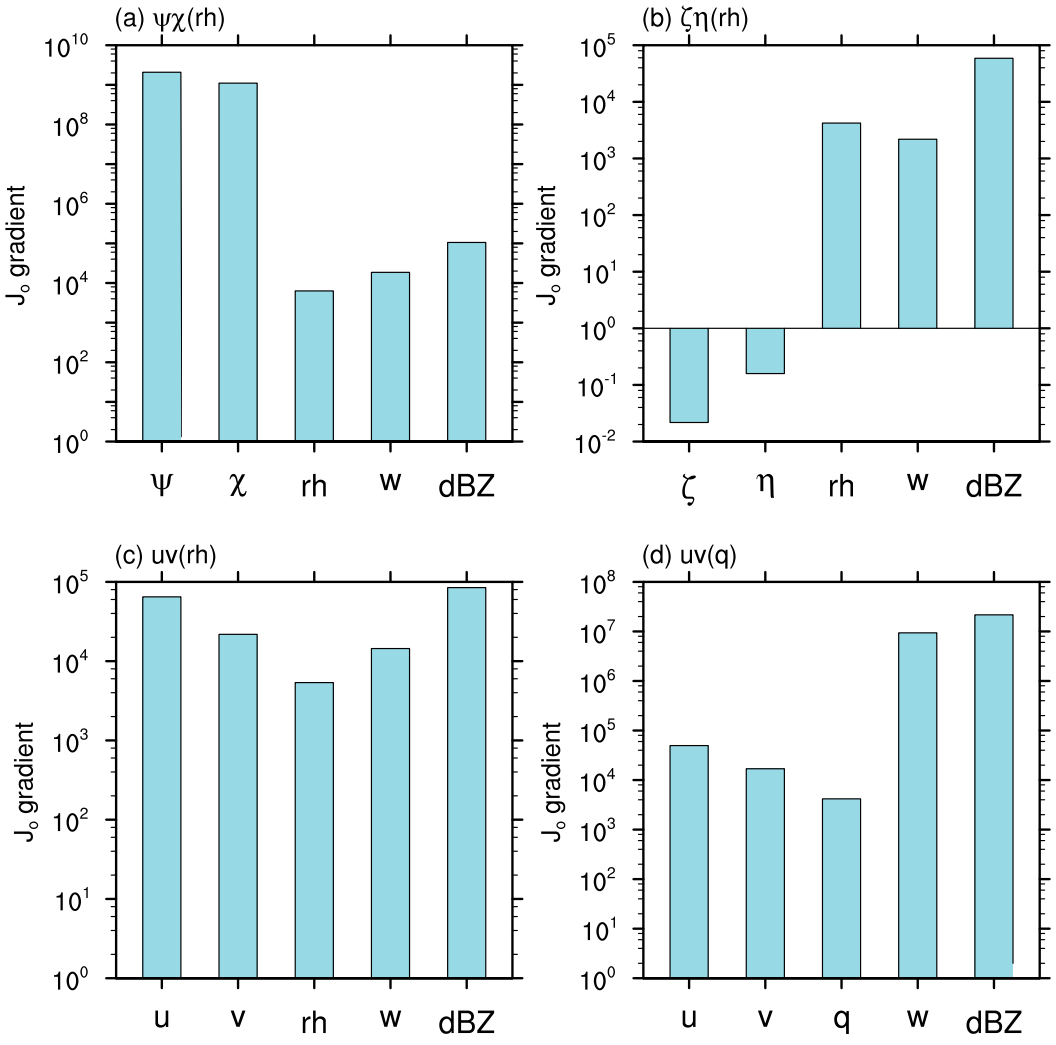

FIG. 4. The J_o gradients (unit: 1) with respect to horizontal momentum CVs, moisture CV, w_u, and dbz_u for (a) CV_$\psi\chi$, (b) CV_$\zeta\eta$, (c) CV_uv, and (d) CV_q. The variable rh_u is used in (a)–(c) as moisture CV, while CV_q adopts uv_u as momentum CVs. CV_rh has the same horizontal momentum and moisture CVs with CV_uv. The J_o gradients are calculated based on the DA cycle valid at 2115 UTC 8 May 2003.

conversely, errors in snow are correlated in horizontal only above the 28th level, and horizontally correlated errors in graupel exist at almost all levels. The horizontal length scale pattern for reflectivity is an integrated consequence over rainwater, snow, and graupel.

To examine the effect of the new static BEC matrix in physical space, a 3DVar experiment is conducted with the assimilation of reflectivity valid at 2115 UTC 8 May 2003. Both first-guess field and the static BEC matrix are from REF. Figure 8 shows that the physically reasonable increments of hydrometeors are produced by adding rainwater below 8 km AGL, graupel across the entire troposphere, and snow above 10 km AGL, respectively. This result suggests that the use of the new static BECs avoids the problem of unphysical increments of hydrometeors discussed in Liu et al. (2019). The added reflectivity corresponds well with the increase of humidity (Fig. 8b) and updraft (Fig. 8a). The increments for horizontal winds are slight (not shown). These increments are produced in agreement with the statistics shown in Fig. 7.

c. *Impact of the inclusion of cross correlations of hydrometeors and vertical velocity with other variables*

To reveal the impact of the inclusion of cross-correlations between hydrometeors/vertical velocity and other variables in the static BECs, three single DA cycle experiments using 3DVar, including an analysis valid at 2115 UTC and a subsequent 5-min forecast valid at 2120 UTC 8 May 2003, are designed (Table 4). In Exp-CNTL, the static BECs adopted is the same as that in REF, which includes correlations of both hydrometeors and w_u with other variables. Exp-noBAL_H uses the same static BECs except omitting the cross-correlations between hydrometeors and other CVs. Reflectivity of Exp-CNTL is ~5 dBZ greater than Exp-noBAL_H at 2115 UTC (Figs. 9a,b). Such reflectivity is missing in the first-guess (not

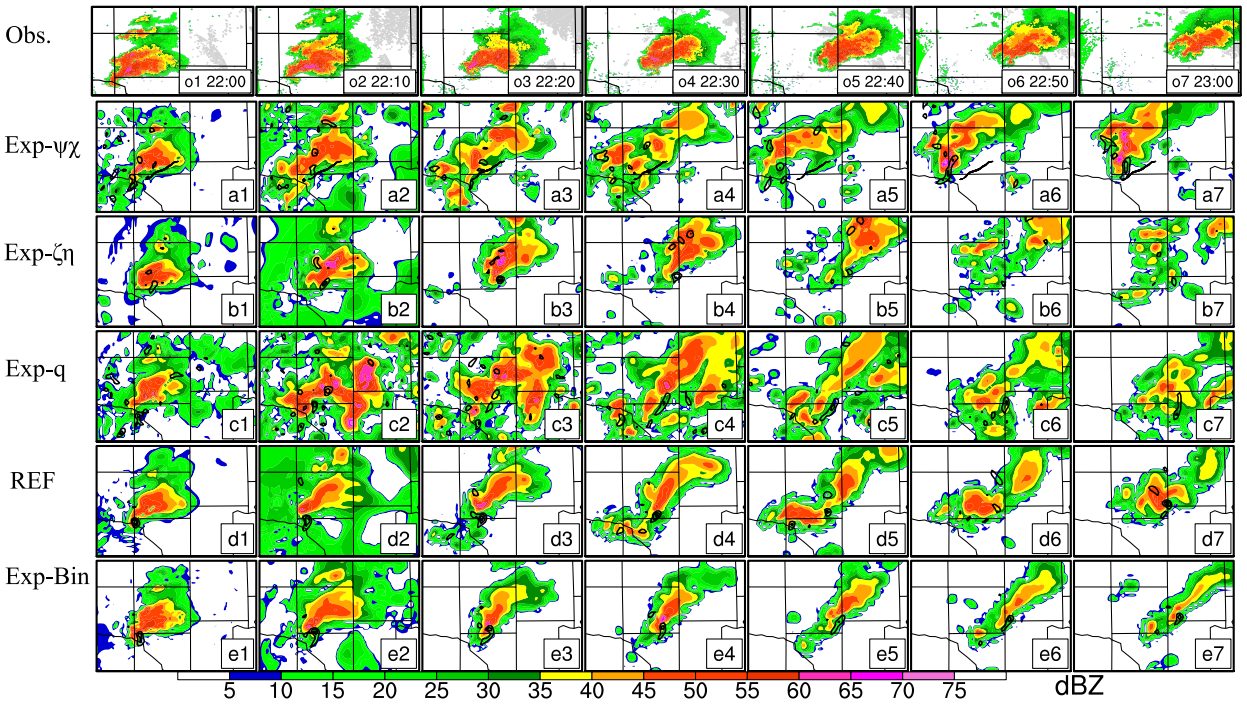

FIG. 5. The reflectivity (colors; dBZ) and vertical vorticity (contours from 0.001 to 0.01 s^{-1} at 0.001-s^{-1} interval) at 1 km AGL for (a1)–(a7) Exp-$\psi\chi$, (b1)–(b7) Exp-$\zeta\eta$, (c1)–(c7) Exp-q, (d1)–(d7) REF, and (e1)–(e7) Exp-Bin. The first column represents the last analysis time valid at 2200 UTC and the second to seventh columns are for the forecast time at 2210, 2220, 2230, 2240, 2250, and 2300 UTC, respectively. The observed reflectivity at corresponding times is also shown in (o1)–(o7).

shown). The analysis in Exp-CNTL has stronger updraft and more saturated relative humidity corresponding to the analyzed reflectivity than Exp-noBAL_H, likely attributed to its more consistent adjustment of vertical velocity and humidity fields (Fig. 9a). Therefore, the convection of Exp-CNTL can be maintained along with the development of a strong updraft during the subsequent forecast (Fig. 9d). However, the added reflectivity in the analysis of Exp-noBAL_H does not correspond to increased humidity (Fig. 9b). At 2120 UTC, much of the added hydrometeors quickly evaporate due to the unsaturated air (Fig. 9e). These results for the 8 May case suggest that the inclusion of cross-correlations between hydrometeors and other variables can be vital in the static BECs for consistently adjusting dynamic and thermodynamic fields.

The impact of adding the cross-correlations between w_u and other variables in the static BECs is examined in the third experiment, Exp-noBAL_W. The static BECs used in Exp-noBAL_W differs from that in Exp-CNTL by skipping the calculation of the balance operators associated with w. All analyzed fields in Exp-noBAL_W (Fig. 9c) are similar with those in Exp-CNTL (Fig. 9a) except the w field, where w in Exp-noBAL_W is 1–3 m s^{-1} weaker than that in Exp-CNTL. At 2120 UTC, Exp-noBAL_W (Fig. 9f) has a weaker updraft than Exp-CNTL (Fig. 9d). Therefore, the corresponding reflectivity core in Exp-CNTL is ~3 dBZ higher than that in Exp-noBAL_W. The reflectivity magnitude in Exp-CNTL is closer to the observations than Exp-noBAL_W (not shown). This result indicates that although most of the storm spinup can be achieved in Exp-noBAL_W (Fig. 9f), the correlations of w_u with other variables additionally favors to produce a variable-coherent analysis and therefore assists accelerating storm spinup in the subsequent forecast of the 8 May case. It noted that including the correlations of w_u with other variables in the static BECs is relatively secondary, compared to including the correlations between hydrometeors and other variables.

d. *Evaluation of binning method for the construction of convective-scale static background-error covariance for direct reflectivity assimilation*

To reveal how the error statistics vary for different storm intensity bins, the cross-variable relationships between reflectivity and rh over the full domain and over the storm areas with varying intensities are represented in Figs. 6b and 6d. Without binning, the reflectivity correlates (correlation value above 0.3) with rh mostly between the 15th and 30th levels (Fig. 6b). In comparison, this cross-correlation inside strong storms is generally enhanced and becomes broader between the 15th and 40th levels and below the 5th level (Fig. 6d). Weak storms have more vertically localized and weaker correlations than strong storms (Fig. 6c). This result is consistent with the stronger and deeper convective processes associated with strong storms. The notably different correlations suggest the need to use different error statistics in areas with varying storm intensities.

We further explore the accumulated effect of the binning through cycled 3DVar experiments. REF has more weak

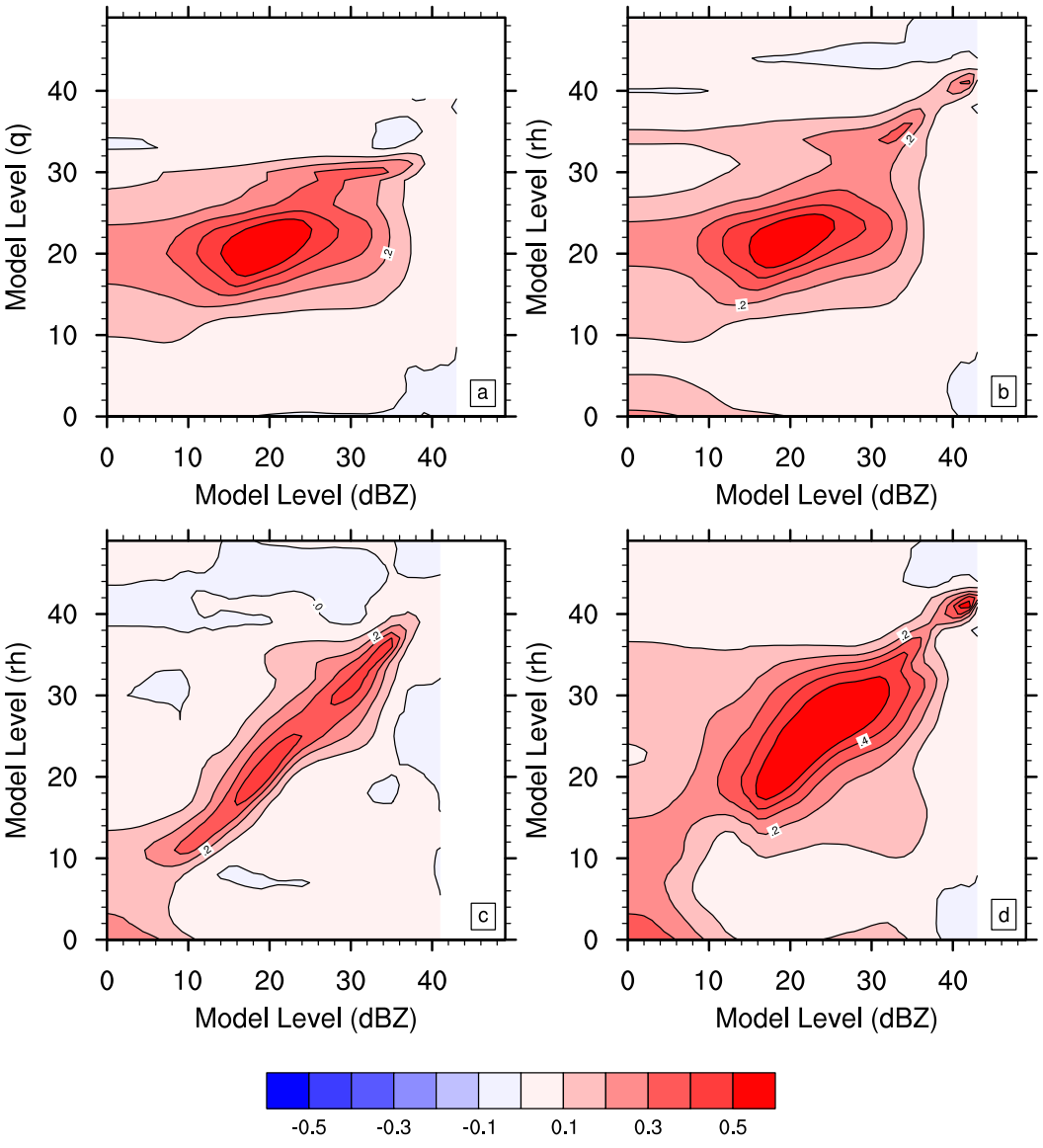

FIG. 6. Vertical cross-variable correlations of model variable reflectivity (dbz) with (a) specific humidity (q) and (b)–(d) relative humidity (rh). The vertical cross-variable correlations are spatially averaged over (b) the entire domain, (c) weak, and (d) strong storms, respectively.

spurious reflectivity and drier air surrounding the primary supercell storm in the first-guess compared to Exp-Bin (Figs. 10a,b). The spurious reflectivity in REF are suppressed in the analysis through assimilating "no-precipitation" observations; however, the corresponding water vapor is unrealistically reduced to be nearly 0 g kg^{-1} (Fig. 10c). In comparison, Exp-Bin does not excessively reduce the moisture when removing spurious reflectivity (Fig. 10d). Similar with Michel et al. (2011), Exp-Bin has a much shorter horizontal error correlation for reflectivity inside the strong storm areas than REF. Specifically, the maximum length of horizontal correlation in Exp-Bin is below 2.5 km, while the maxima in REF reaches 6.0 km. Therefore, the spurious reflectivity in REF is likely because the updated storm information spreads over clear-air areas through the effect of a wider spatial error correlation in the preceding cycle's analysis. In contrast, the added storm information in Exp-Bin is confined due to the shorter horizontal correlation inside the storm areas. When suppressing spurious reflectivity in DA procedure, the strong coupling of reflectivity with rh indicated in Fig. 6b leads to the excessive reduction of moisture in REF, while the moisture in Exp-Bin is properly adjusted based on the error statistics from the clear-air bin with a weak correlation between reflectivity and rh (not shown). Diagnostics for Fig. 10 suggest that Exp-Bin can alleviate the generation of spurious reflectivity and the excessive reduction of moisture when suppressing the spurious reflectivity, relative to REF.

Reflectivity analyses from both experiments reproduce the hook-echo structure at approximately the correct location

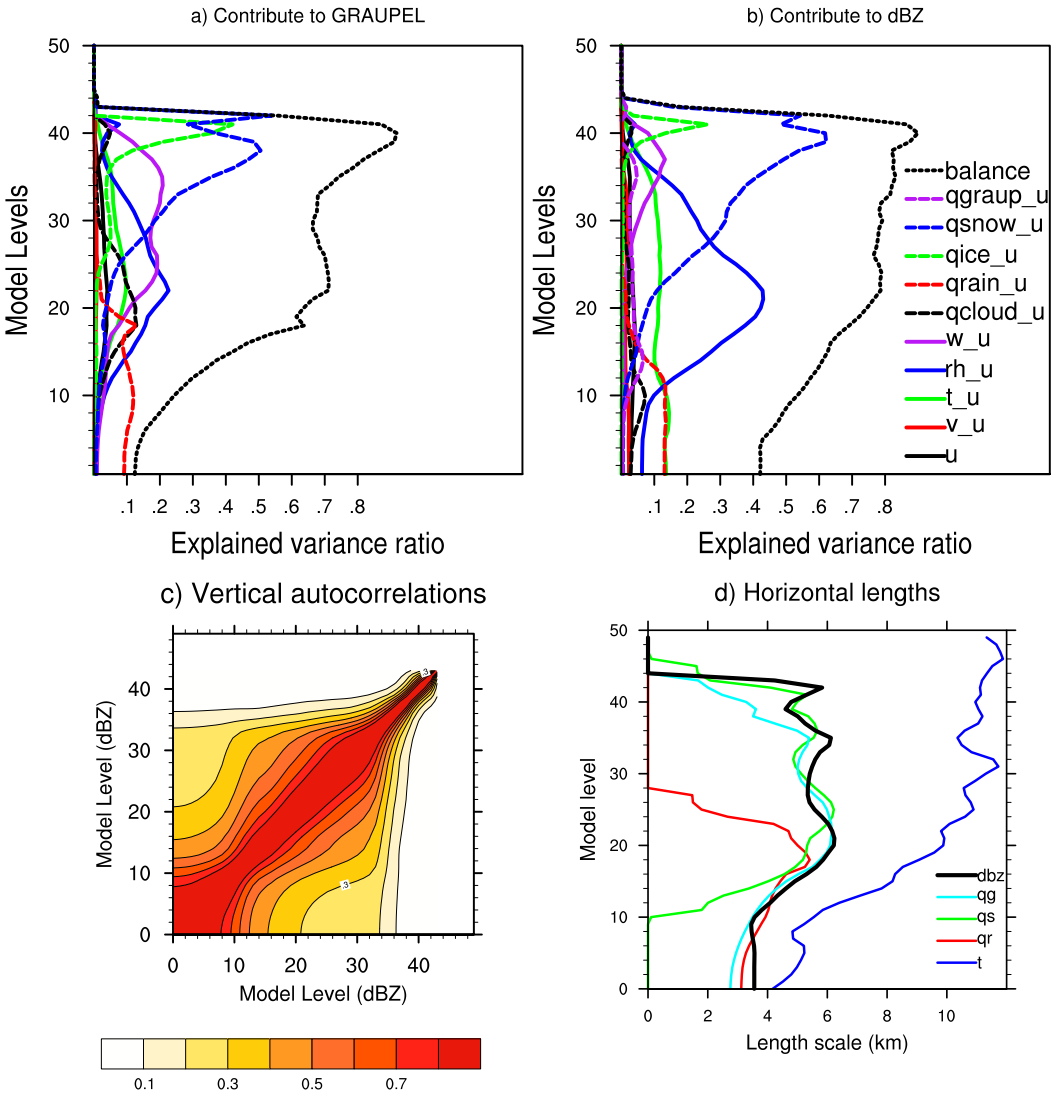

FIG. 7. Explained-variance ratio of (a) graupel and (b) reflectivity (dBZ) as a function of model level. (c) Average vertical autocorrelations for reflectivity (dBZ) as a function of model level. (d) Horizontal length scales (km) as a function of model level for reflectivity (dbz), graupel (qg), snow (qs), rainwater (qr), and temperature (t). The ratio of the explained variance relative to the total variance is "balance" shown in (a) and (b).

[Figs. 5d(1),e(1)]. Both experiments also produce the strong low-level rotation at 1 km AGL, with REF showing slightly stronger vorticity than Exp-Bin. An isolated storm with the low-level vorticity greater than 0.002 s^{-1} persists in Exp-Bin during the entire 1-h forecast period, despite its reflectivity in the forward-flank region weakens at 2300 UTC [Fig. 5e(7)]. In comparison, REF enhances spurious storms in southwest of the main storm from 2230 UTC [Fig. 5d(4)] and dissipates reflectivity in the forward-flank regions at 2300 UTC [Fig. 5d(7)]. The low-level rotation of REF also dissipates and is replaced by that associated with the spurious storms at 2240 UTC [Fig. 5d(5)]. At 4 km AGL, Exp-Bin and REF produce similar midlevel mesocyclones with the maximum updraft greater than 25 m s^{-1} and the vorticity maxima exceeding 0.008 s^{-1} at 2200 UTC [Figs. 11a(1),b(1)]. During the forecast, Exp-Bin further extends the persistence of the storm beyond 2300 UTC [Fig. 11b(7)] relative to REF, although its maximum updraft and vorticity get weakened after 2240 UTC. In REF, the midlevel mesocyclone dissipates at 2240 UTC [Fig. 11a(5)], followed by several weak spurious cells [Figs. 11a(5)–a(7)]. Overall, Exp-Bin produces a more realistic analysis, predicts the storm with its storm morphology closer to the reality, and persists the strong midlevel mesocyclone for a longer duration, relative to REF.

e. *Effect of hybridizing static and ensemble background-error covariance in hybrid EnVar for direct reflectivity assimilation*

As expected, direct reflectivity assimilation using 3DVar with the constructed static BECs efficiently and effectively

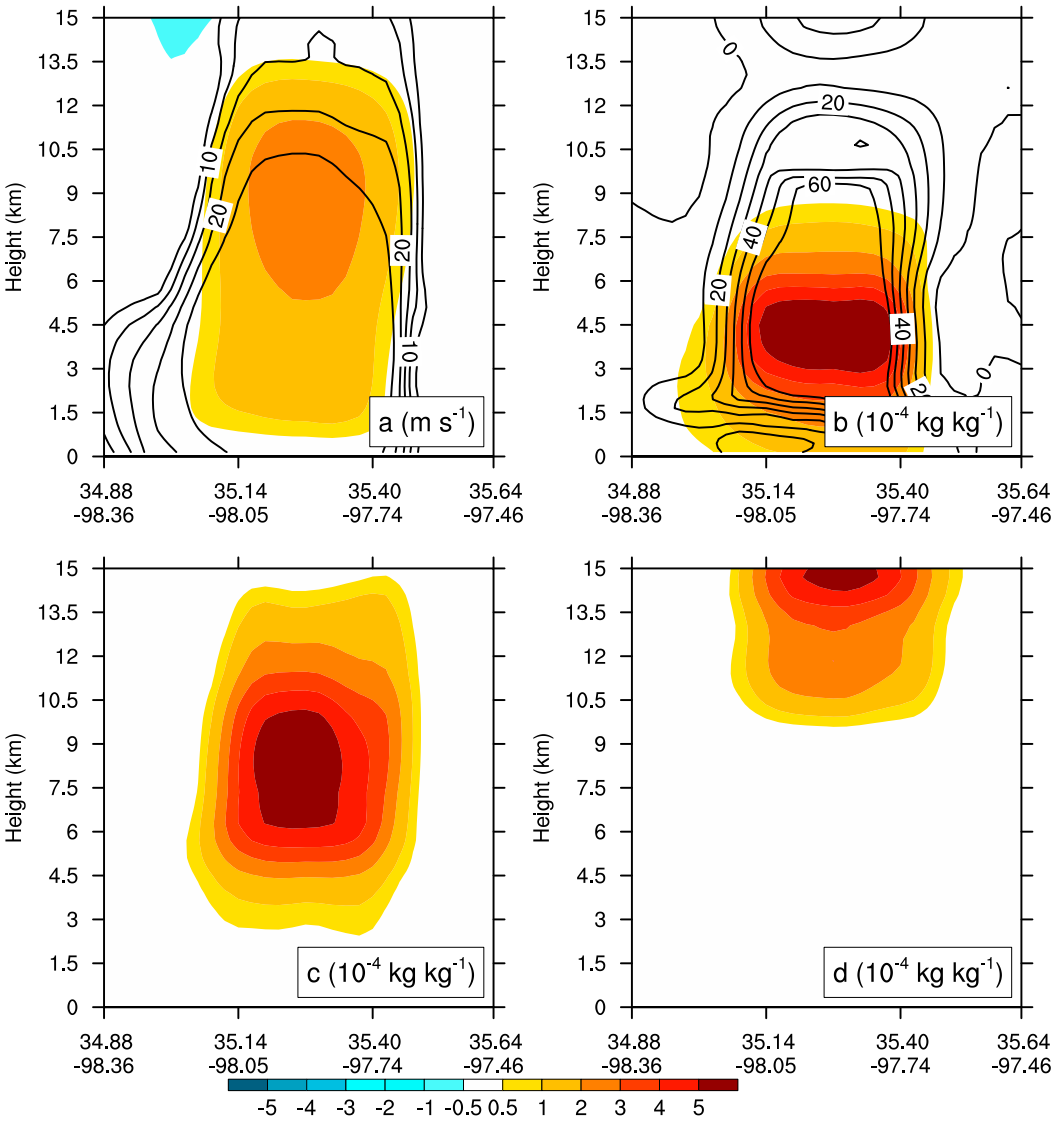

FIG. 8. Vertical cross sections of analysis increments of (a) vertical velocity (colors; m s^{-1}) and reflectivity (contours from 5 to 30 dBZ at 5-dBZ intervals; dBZ), (b) rainwater (colors; kg kg^{-1}) and relative humidity (contours from 0% to 80% at 10% interval), (c) graupel (colors; kg kg^{-1}), and (d) snow (colors; kg kg^{-1}) across the strong updraft core valid at 2115 UTC 8 May 2003. Both colors and contours represent the analysis increments.

adds storms for the 8 May 2003 OKC supercell in Exp-Bin. Note that the predicted supercell storm in the 3DVar Exp-Bin experiment still deviates from the reality for intensity and reflectivity morphology. Early studies suggest that the hybrid EnVar can leverage the benefits of both static and ensemble BECs (X. Wang et al. 2007a, 2008a, 2009, 2013; Li et al. 2012; Gao et al. 2013; Gao and Stensrud 2014; Schwartz 2016; Kong et al. 2018; Montmerle et al. 2018; Wang et al. 2019). This section therefore performs hybrid EnVar experiments to 1) examine the effect of adding static BEC on top of the ensemble covariance and to 2) explore if hybrid EnVar has benefits over 3DVar with the new static BECs. Optimizations of the convective-scale static BECs in sections 4a and 4d are also valid in hybrid EnVar. We use the adaptive hybridization, in addition to the optimized static BECs, in both hybrid experiments of Table 3.

1) DA CYCLING

Figure 12 provides the root-mean-square fit to observations (RMSF) used to quantify the effect of including static BECs during the hybrid DA cycling. The RMSF of both prior and posterior in Exp-PureEnVar are larger than those in two hybrid experiments, especially for the reflectivity observations. The closer fit of the posterior to the reflectivity in hybrid experiments confirms that the constructed static BECs can efficiently add reflectivity in the analysis. The ability of this static BECs to add reflectivity is further indicated by the better fit of the prior to the reflectivity observations in the subsequent

TABLE 4. List of the configuration of static BECs in sensitivity experiments.

Expt	Static BECs configuration
Exp-CNTL	Inclusion of correlations of hydrometeors and vertical velocity with other variables
Exp-noBAL_H	Same as Exp-CNTL but without the correlation between hydrometeors and other variables
Exp-noBAL_W	Same as Exp-CNTL but without the correlation between vertical velocity and other variables

15-min forecasts, as those added reflectivity is well maintained (Fig. 12b). Both forecasts and analyses in two hybrid experiments better fit radial velocity observations than in Exp-PureEnVar at 2200 UTC. The RMSF of the posterior in Exp-hyb0.3 is slightly less than that in Exp-hyb0.1 for reflectivity observations. Exp-hyb0.1 and Exp-hyb0.3 comparably fit the radial velocity observations. Despite both hybrid experiments has slightly larger spread for reflectivity at 2130 and 2145 UTC than Exp-PureEnVar, the total spreads for both radial velocity and reflectivity are still smaller than the RMSF in all three experiments. This result indicates that the ensemble is underdispersive during all DA cycles. By the design of the adaptive hybridization (section 2c), the static BECs are therefore applied to the entire storm regions.

Figure 13 shows the effect of static BECs on the reduction of the spinup during DA cycling. Exp-PureEnVar fails to add reflectivity at 2115 and 2130 UTC (Figs. 13e,f) as a result of all the ensemble members failing to produce the observed storm. Until 2145 UTC, some spotted reflectivity is analyzed (Fig. 13g). The reflectivity analysis still largely deviates from the observations in size and shape at 2200 UTC, as the forward-flank region of the observed storm are missed by all ensemble background members (purple lines in Fig. 13h). This result indicates that Exp-PureEnVar requires a spinup time beyond the 1-h period. In comparison, both Exp-hyb0.1 and Exp-hyb0.3 efficiently add some reflectivity at 2115 UTC (Figs. 13i,m), with their intensity much weaker than the reality. Both hybrid experiments reach their stable reflectivity value at 2145 UTC (Figs. 13k,o), which shows that the spinup time in both hybrid experiments is notably reduced. At 2200 UTC, the reflectivity

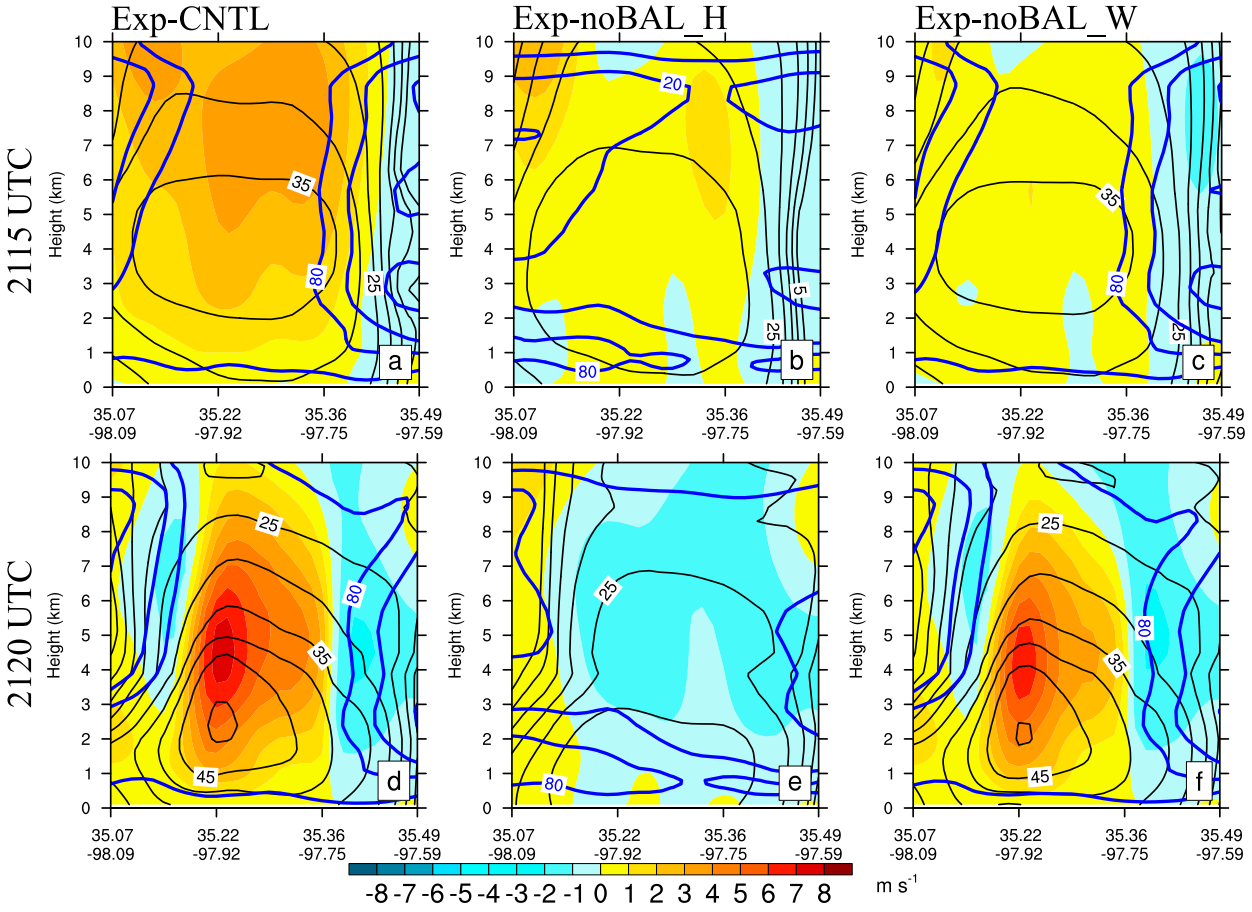

FIG. 9. Vertical cross sections of vertical velocity (colors; m s^{-1}), reflectivity (black contours from 5 to 50 dBZ at 5-dBZ intervals; dBZ), and relative humidity (blue contours from 20% to 80% at 30% interval) for (top) analyses at 2115 UTC and (bottom) 5-min forecasts at 2120 UTC 8 May 2003 from (a),(d) Exp-CNTL; (b),(e) Exp-noBAL_H; and (c),(f) Exp-noBAL_W.

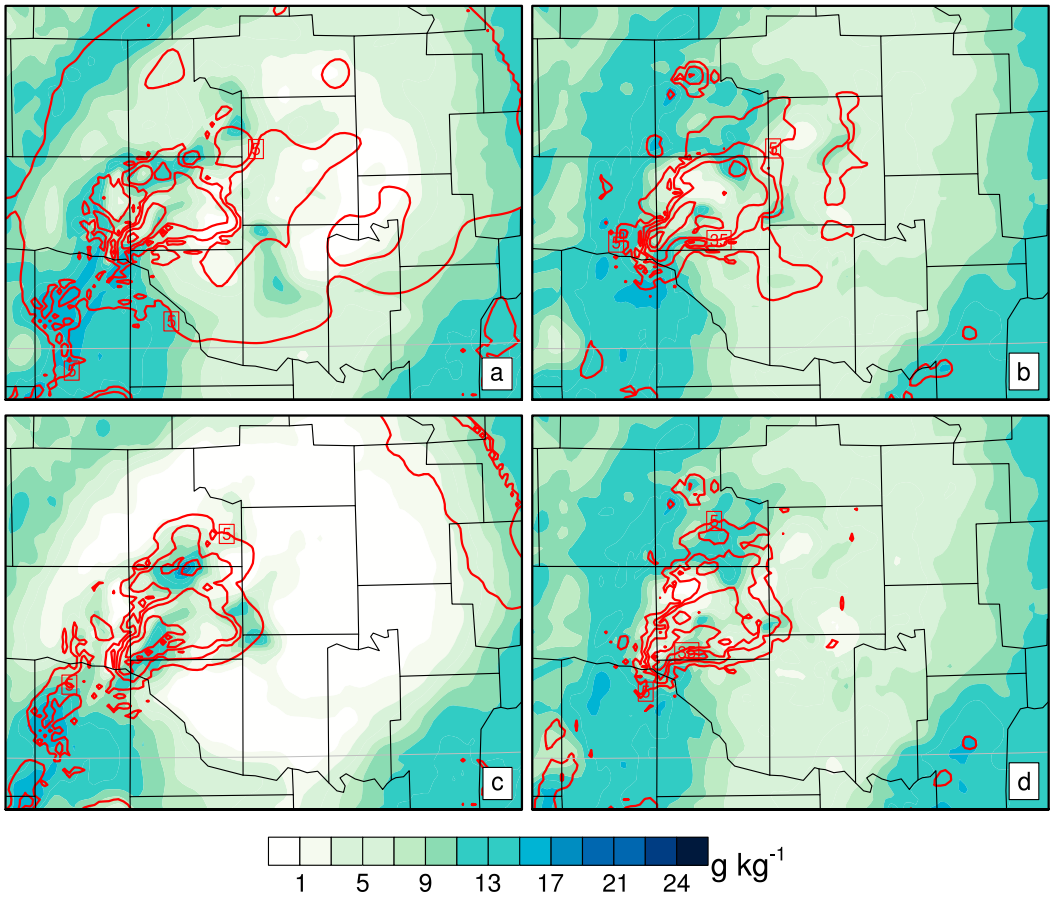

FIG. 10. Water vapor mixing ratio (colors; 2 g kg^{-1} interval) and reflectivity (contours, starting from 5 dBZ with a 15-dBZ interval) at 1.5 km AGL in (a),(b) first-guess and (c),(d) analysis valid at 2200 UTC from (left) REF and (right) Exp-Bin.

distributions in both Exp-hyb0.1 and Exp-hyb0.3 (Figs. 13l,p) compare well with the size and shape of the observed reflectivity (Fig. 13d). Moreover, both hybrid experiments outperform Exp-PureEnVar in reproducing the hook-echo structure. Consistent with Fig. 12, the difference between Exp-hyb0.1 and Exp-hyb0.3 shown in Figs. 13l and 13p is small. The 3DVar Exp-Bin experiment (Fig. 5e1) has comparable reflectivity analyses with both hybrid experiments

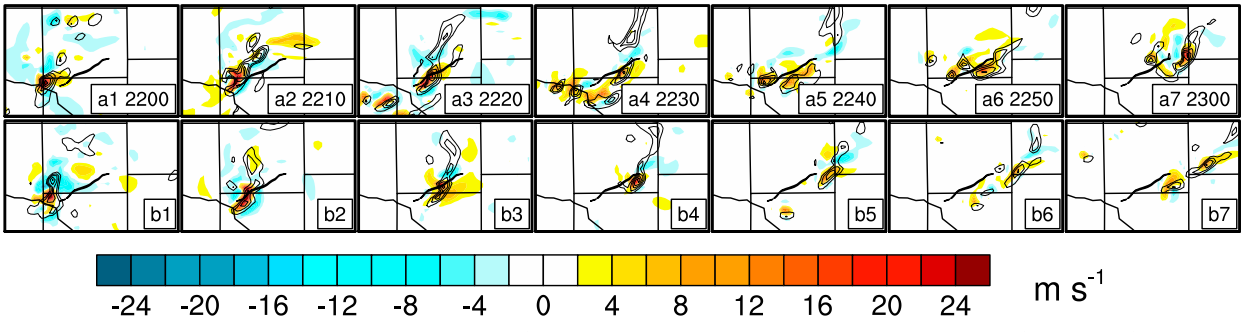

FIG. 11. The evolution of vertical velocity (colors; m s^{-1}) and vertical vorticity (contour starting from 0.002 s^{-1} at 0.002 s^{-1} interval) at 4 km AGL during a 1-h forecast period starting from the analyses at 2200 UTC and ending at 2300 UTC from (a1)–(a7) REF and (b1)–(b7) Exp-Bin. The first column represents the last analysis time valid at 2200 UTC and the second to seventh columns are for the forecast time at 2210, 2220, 2230, 2240, 2250, and 2300 UTC, respectively. The overlaid line in each panel is the NWS observed tornado damage tracks during 2204–2208 and 2210–2238 UTC.

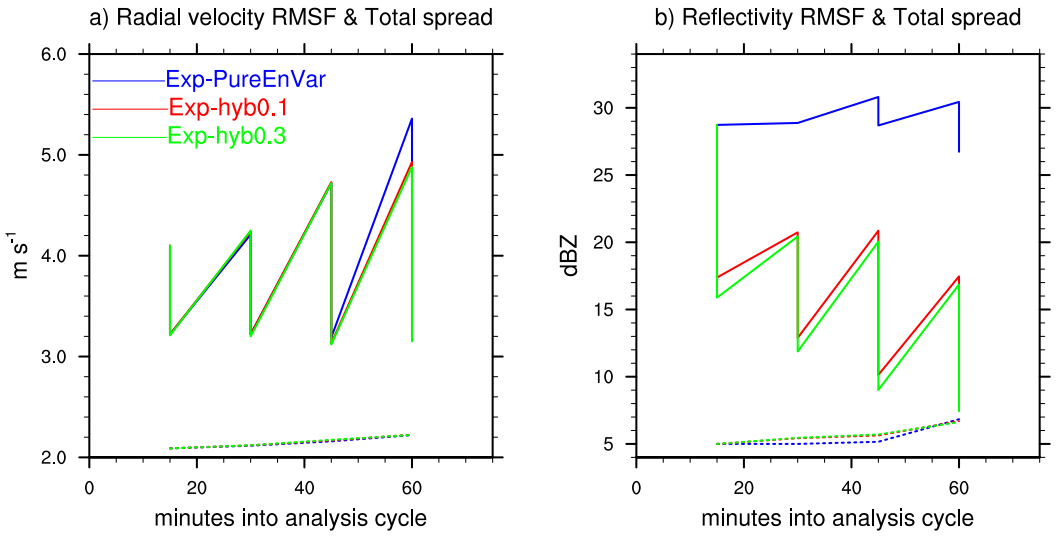

FIG. 12. The RMSF (solid) and total spread (dash) statistics in observation-space diagnostics for the assimilated KTLX (a) radial velocity and (b) reflectivity for Exp-PureEnVar (blue), Exp-hyb0.1 (red), and Exp-hyb0.3 (green). The RMSF statistics for the first guess and analysis are, respectively, shown in the upper points and lower points of the sawtooth patterns in (a) and (b). The total spread for the first guess is also provided.

(Figs. 13l,p) at 2200 UTC. All of them capture the storm much better than Exp-PureEnVar.

2) FORECASTS

Although all experiments predict an isolated storm during the entire forecast period, important differences remain in the forecasts. Exp-hyb0.1 and Exp-hyb0.3 show comparable reflectivity throughout the forecast that are closer to the observations than Exp-PureEnVar, especially before 2230 UTC. In particular, these hybrid experiments outperform Exp-PureEnVar with a larger spatial coverage of strong reflectivity in the forward flank region and a stronger low-level rotation (Figs. 14i–j,m–n). Strong low-level rotations above $0.002\,s^{-1}$ persist during the entire 1-h forecast period for Exp-hyb0.1 and Exp-hyb0.3; in contrast, vorticity maxima are below $0.002\,s^{-1}$ for Exp-PureEnVar at most forecast lead times (Figs. 14e–h). At 4 km AGL, the forecasts of updraft and vorticity from Exp-hyb0.1 and Exp-hyb0.3 are very similar, while that of Exp-PureEnVar is weaker ($1–3\,m\,s^{-1}$ and $0.002\,s^{-1}$) than both hybrid experiments at 2210 UTC [Figs. 15a(2),b(2),c(2)] and after 2240 UTC [Figs. 15a(5)–a(7),b(5)–b(7),c(5)–c(7)].

Both hybrid experiments also improve upon pure 3DVar Exp-Bin for reflectivity coverage at 2300 UTC [Figs. 5e(7) vs 13l,p], suggesting the positive impact of inclusion of ensemble covariance. At midlevel, the mesocyclone in Exp-Bin is gradually weakening after 2240 UTC [Figs. 11b(5)–b(7)] where the maximum updraft is reduced from above $25\,m\,s^{-1}$ to under $10\,m\,s^{-1}$. In contrast, all EnVar experiments in Table 3 maintain a much stronger mesocyclone than Exp-Bin [Figs. 15a(5)–(7),b(5)–(7),c(5)–(7)], with the maximum updraft consistently exceeding $19\,m\,s^{-1}$.

For a quantitative evaluation, Fig. 16 shows the RMSF of radial velocity and reflectivity at a 5-min interval during 2200–2300 UTC. During 2200–2220 UTC, Exp-Bin, Exp-hyb0.1, and Exp-hyb0.3 have 6–19 dBZ smaller reflectivity RMSF than Exp-PureEnVar and such advantage is maintained throughout the 1-h forecast period (Fig. 16b). For the radial velocity RMSF, both hybrid experiments perform consistently better than Exp-Bin and Exp-PureEnVar during the entire forecast period (Fig. 16a). Overall, Exp-PureEnVar has the largest reflectivity RMSF due to its ensemble deficiency (Fig. 12b); the hybrid experiments blending the ensemble and static BECs produce overall better convective-scale forecasts than the pure 3DVar and EnVar.

3) FURTHER EXAMINATION USING THE 20 MAY 2013 OKLAHOMA SUPERCELLS

Experiments for an additional 20 May 2013 multisupercell case confirm the selection of horizontal momentum and moisture CVs for the 8 May 2003 case (not shown). This case is also used to further examine the impact of the newly constructed convective-scale static covariances, and to demonstrate the effect of the adaptive hybridization. The impact of the static BECs in hybrid EnVar is further demonstrated through experiments in Table 3 for this case with a DA period of 1915–45 UTC at a 15-min interval. As discussed in section 4e(1), most early cycles during the DA cycling period for the 8 May 2003 case dominate by most or all ensemble members failing to sample the observed storm. Even at the final analysis time (2200 UTC), all ensemble members miss the forward-flank of this observed storm (purple lines in Fig. 13h). In contrast, the 20 May 2013 case includes cycles where the background ensemble is much improved. For example, like at 1945 UTC, indicated by the purple lines in Fig. 17a(1), the ensemble is underdispersive, but most ensemble members do not miss the observed storms. Similar qualitative differences in reflectivity between two experiments as the 8 May case are produced in analysis and prediction. Similar reflectivity distributions are

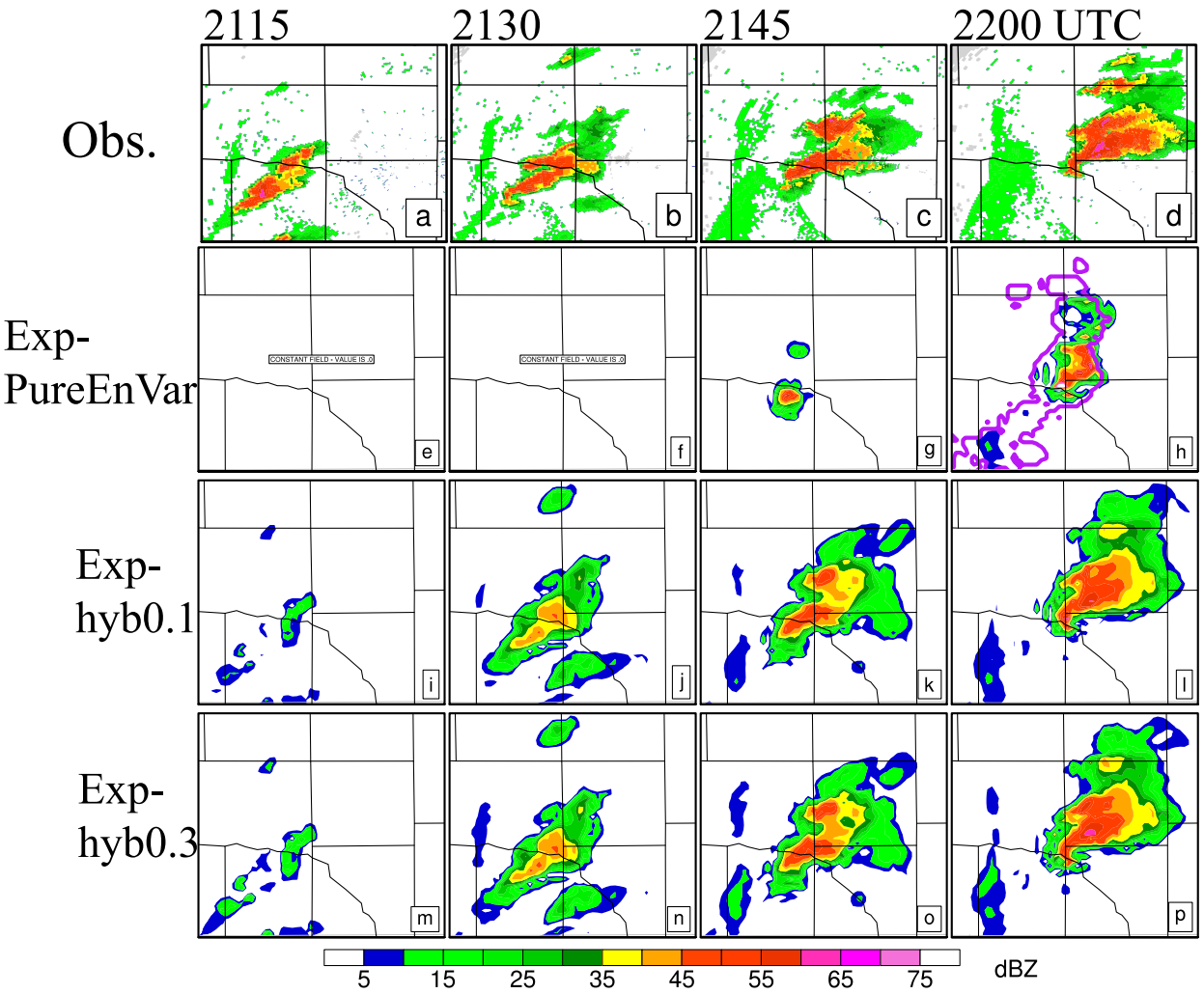

FIG. 13. The reflectivity analysis at 1 km AGL for (e)–(h) Exp-PureEnVar, (i)–(l) Exp-hyb0.1, and (m)–(p) Exp-hyb0.3 from each data assimilation cycle during the entire 1-h DA period. (a)–(d) The observed reflectivity at corresponding times is also shown. The purple outline in (h) indicates the locations where any ensemble member has reflectivity exceeding 10 dBZ at 1 km AGL valid at 2200 UTC.

predicted in Exp-hyb0.1 [Figs. 17b(1)–b(5)] and Exp-hyb0.3 [Figs. 17c(1)–c(5)]. Their reflectivity distribution compares well with the size and shape of the observed reflectivity, especially for the storm A and B. In contrast, Exp-PureEnVar produces multicellular convective storms rather than supercells in Figs. 17a(1)–a(5). For the storm C, all experiments fail to predict it after 2000 UTC [Figs. 17a(2),b(2),c(2)].

For the 8 May 2003 case in section 4e(1), given the large ensemble background deficiency during a few early DA cycling period, the adaptive hybridization approach ends up assigning static BECs for all storm regions. To further examine the adaptive hybridization, we further extend the DA cycling to 2000 UTC for the 20 May 2013 case, design and conduct three experiments (Table 5). Analyzed reflectivity by Exp-PureEnVar captures most storms [Figs. 17o(2),d(1)]. This result suggests that its ensemble prior at 2000 UTC samples the background errors properly for most of the storms. As expected, Exp-Adaptive using the adaptive hybridization allows the static BECs to be incorporated only at limited regions, indicated by the black contours in Fig. 17e(1). The reflectivity analyses in Exp-PureEnVar and Exp-Adaptive are similar, except that some reflectivity patches in the edge of storm B, C are precisely added by Exp-Adaptive through using the static BECs [Fig. 17e(1)]. At 2015 UTC, Exp-Adaptive slightly outperforms Exp-PureEnVar in the forward-flank of storm B [Figs. 17o(3),d(2),e(2)]. After that, comparable reflectivity forecasts for the storm A–C are produced by Exp-PureEnVar and Exp-Adaptive [Figs. 17d(3)–d(4),e(3)–e(4)]. In contrast to Exp-Adaptive, Exp-NoAdaptive uses the hybridized BECs on the whole computational domain. Relative to Exp-Adaptive, Exp-NoAdaptive overly enhances the reflectivity for all storms and produces some spurious weak reflectivity surrounding the primary storms [Fig. 17f(1)]. Forecasts by Exp-Adaptive have the reflectivity distributions in size and shape closer to the observations for storm B, C after 2030 UTC [Figs. 17e(3)–e(4)] than by Exp-NoAdaptive, which obtains

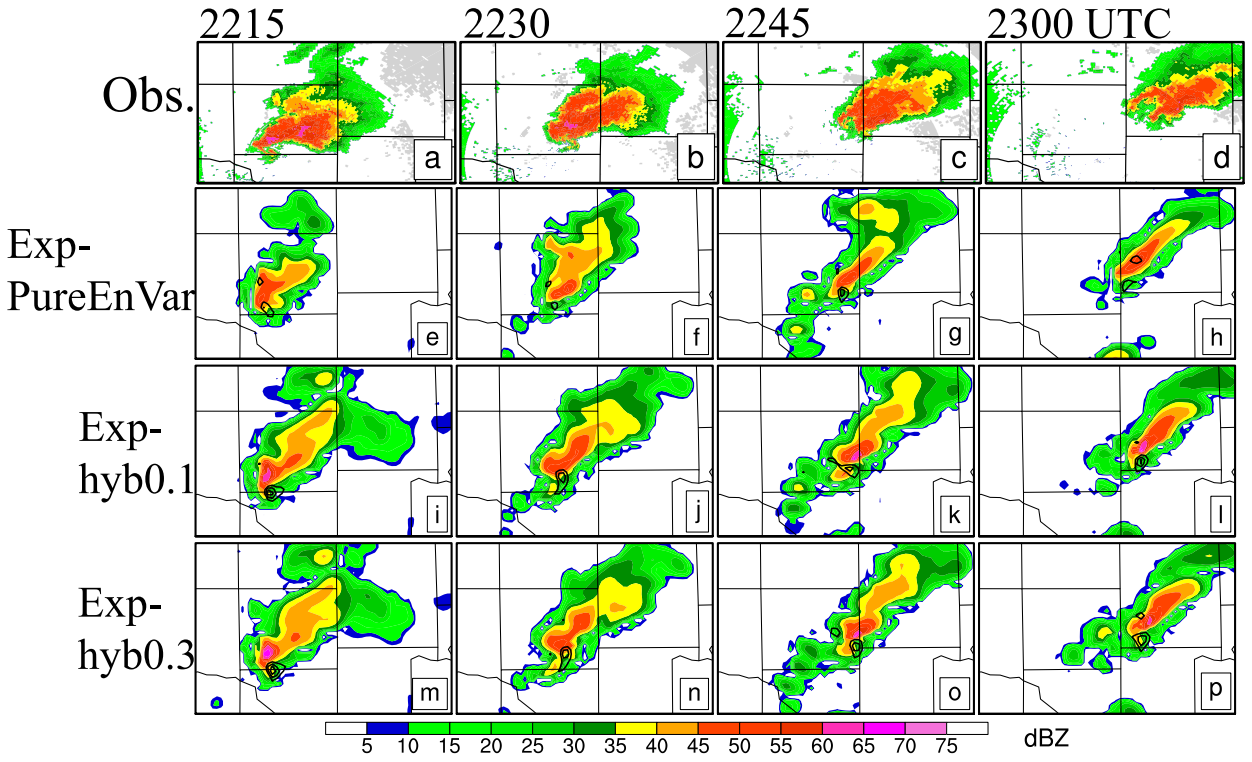

FIG. 14. As in Fig. 5, but for (e)–(h) Exp-PureEnVar, (i)–(l) Exp-hyb0.1, and (m)–(p) Exp-hyb0.3 during 2215–2300 UTC every 15 min.

weakening storm B, C with shrinking reflectivity coverages from 2030 UTC [Figs. 17f(3)–f(4)]. The results for 20 May 2013 and the 8 May 2003 case collectively show the benefits of the adaptive hybridization and static BECs when the ensemble suffers from its deficiency in sampling the forecast errors. Additional examinations of these developments will be required for more robust conclusions using more cases.

5. Summary and discussion

In this study, the static background-error covariance (BEC) matrix is further developed for convective-scale direct radar reflectivity assimilation. It is then implemented and tested within the GSI-based 3DVar and hybrid EnVar framework. Major developments for the static BECs include four aspects. First, the static BEC matrix is extended to include all hydrometeor types, vertical velocity, and reflectivity as control variables (CVs). Linear regressions among all CVs including those newly extended CVs are calculated to model the multivariate error covariances for convective scales. Second, a storm intensity-dependent binning method is adopted to separately calculate the static BEC matrices for clear-air and storms with varying intensities. During the variational minimization, these different static BEC matrices are simultaneously applied at proper locations guided by the observed reflectivity. Third, an adaptive hybridization is implemented so that the static BEC is included in hybrid EnVar only when ensemble covariances demonstrate deficiencies, measured here by consistency ratios less than α, where $0 < \alpha \leq 1$. Fourth, several options of horizontal momentum and moisture CVs are included for the purpose of selecting the appropriate CVs for convective-scale radar DA.

The Oklahoma City (OKC) tornadic supercell storm occurring on 8 May 2003 is first used to examine and evaluate various aspects of the newly extended static BECs through running diagnostics with 3DVar. First, $u v$ and rh are identified as the selected horizontal momentum and moisture CVs, respectively, by comparing with other CVs choices. They avoid the large discrepancy of the cost function gradient among CVs. Such discrepancy is present in other CV options and leads to inefficient convergence in the minimization. The 3DVar experiments suggest that the predicted tornadic supercell with the use of $u v$ and rh as CVs maintains the strong midlevel updraft and vorticity beyond 2215 UTC, while $\psi\chi$, $\zeta\eta$, and q as CVs fail to accurately initialize the storm at the analysis time. Second, the benefits of the inclusion of cross-correlations of hydrometeors and vertical velocity with other variables on the maintenance of the analyzed storms and the acceleration of the storm spinup are demonstrated using the new static BECs. Including correlations between hydrometeors and other variables shows more benefit compared to those between vertical velocity and other variables. Third, the storm intensity-dependent binning allows more appropriate coupling between reflectivity and other variables within storms. In the 3DVar DA cycling, the binning (Exp-Bin) alleviates the generation of spurious reflectivity and the excessive reduction of moisture when suppressing spurious reflectivity compared to without the binning (REF). Compared to REF,

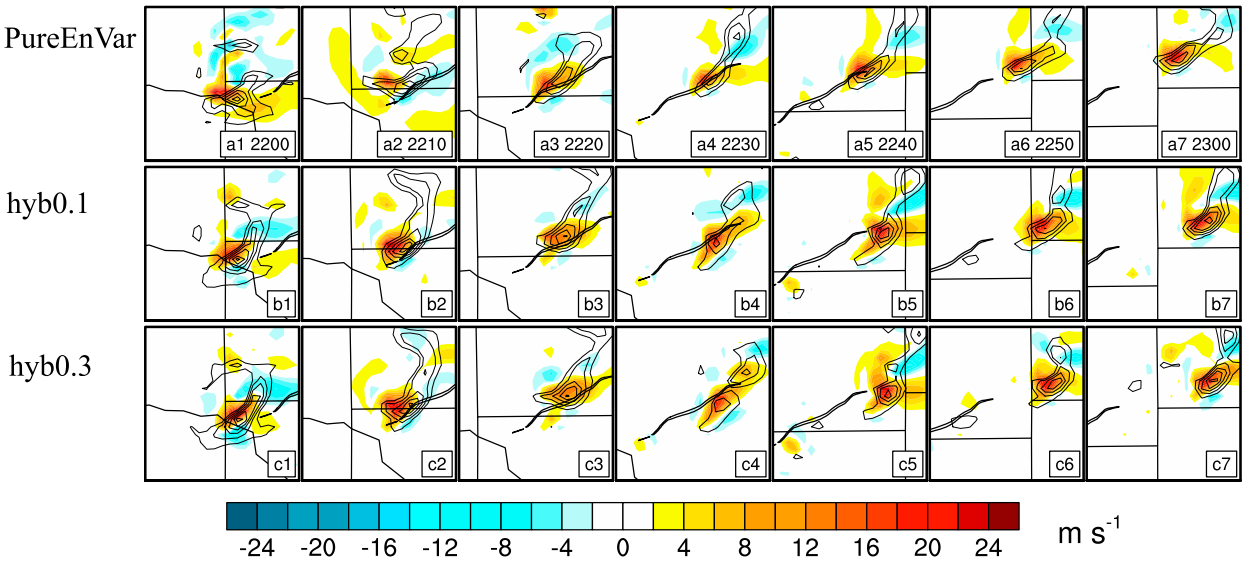

FIG. 15. As in Fig. 11, but for (a1)–(a5) Exp-PureEnVar, (b1)–(b5) Exp-hyb0.1, and (c1)–(c5) Exp-hyb0.3 during a 1-h forecast period starting from 2200 to 2300 UTC at 15-min interval.

Exp-Bin produces a more realistic analysis, predicts the storm with its proper characteristics (i.e., the hook echo, and the reflectivity shape in the forward-flank) closer to the reality, and persists the strong midlevel mesocyclone for a longer duration.

The effectiveness of the new static BECs is further examined in the GSI-based hybrid EnVar system first for the 8 May 2003 case and then with an additional 20 May 2003 multisupercell case. For the 8 May 2003 case, three experiments are conducted and compared. The BEC is fully provided by the ensemble covariance in Exp-PureEnVar. Two hybrid experiments, Exp-hyb0.1 and Exp-hyb0.3, use a blended BEC matrix with a static covariance weight of 10% and 30%, respectively. During DA cycling, both hybrid experiments produce first guesses and analyses better fitting to the reflectivity observations, relative to Exp-PureEnVar. Increasing the static covariance weight in Exp-hyb0.3 slightly enhances the magnitude of reflectivity analysis compared to Exp-hyb0.1 as shown in the RMSF. During the forecast, both hybrid experiments perform similarly, and outperform Exp-PureEnVar in the spatial coverage of reflectivity, the hook-echo structure and the midlevel updraft and vorticity. The benefit of hybrid experiments relative to Exp-PureEnVar is a result of the poor sampling of the background ensemble on the observed storms. Compared to the pure 3DVar experiment with the new static covariances, both hybrid EnVar experiments also have more accuracy in the reflectivity coverage at 2300 UTC, and in the persistence of the strong midlevel mesocyclone from 2240 UTC. Quantitively, both hybrid experiments perform better than the pure 3DVar and EnVar in terms of the 1-h forecasts of radial velocity and reflectivity. Overall, these results suggest the hybrid EnVar leverages the strength of both the static and ensemble BECs. Further examination on the 20 May 2013 Oklahoma supercells demonstrates the adaptive hybridization method serves as expected to apply the static BECs only where ensemble has deficiencies and a similar positive impact of the static

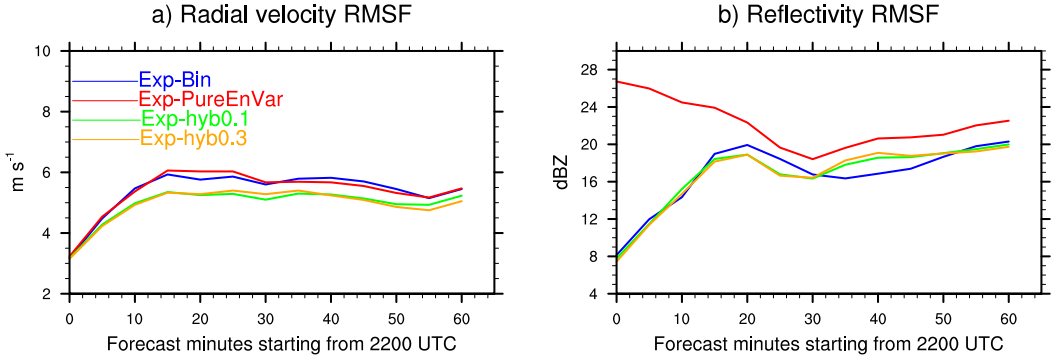

FIG. 16. RMSFs of the KTLX (a) radial velocity and (b) reflectivity for Exp-Bin (blue), Exp-PureEnVar (red), Exp-hyb0.1 (green), and Exp-hyb0.3 (yellow) during 2200–2300 UTC.

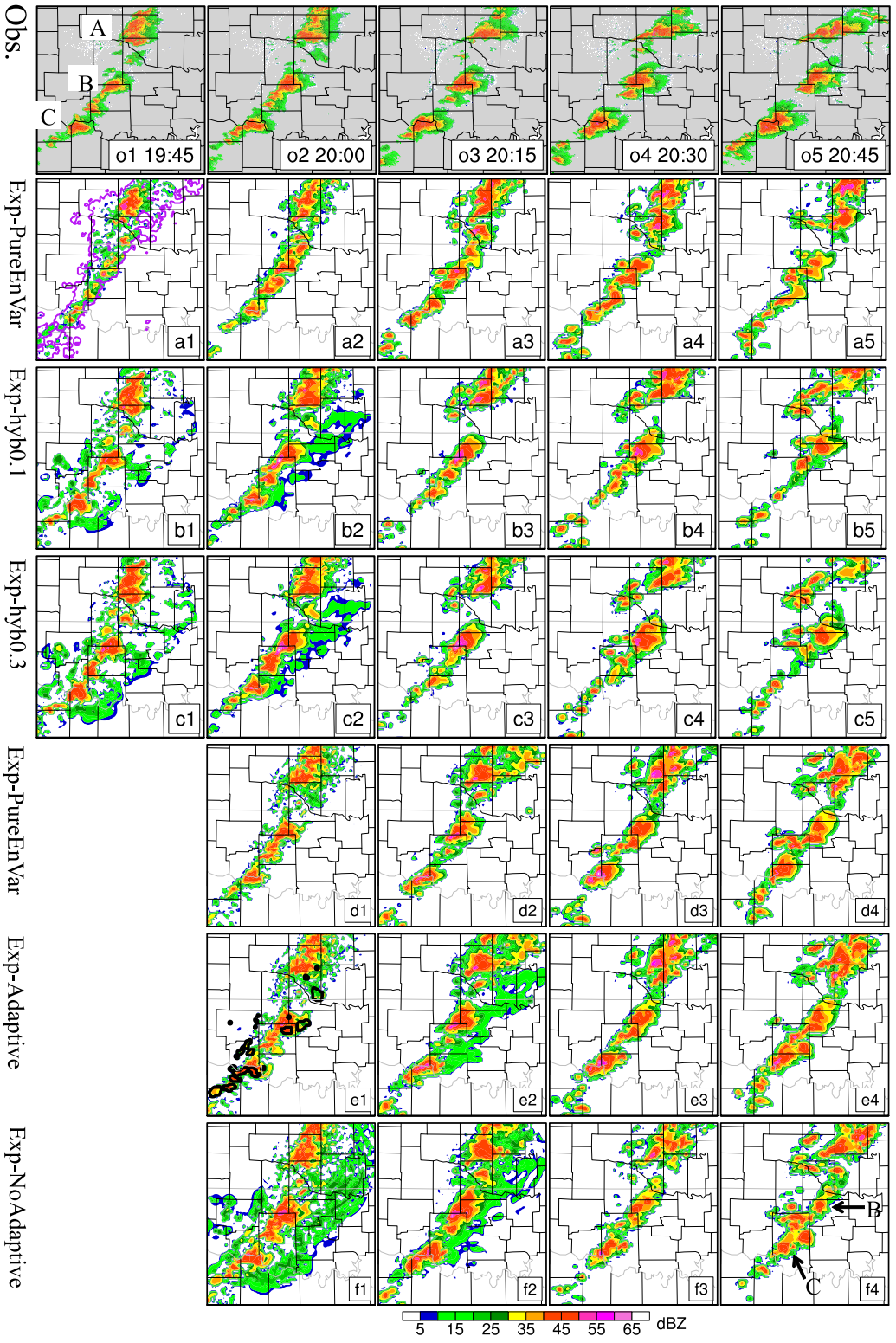

FIG. 17. As in Fig. 12, but for the 1-h forecasts initialized at 1945 UTC from (a1)–(a5) Exp-PureEnVar, (b1)–(b5) Exp-hyb0.1, (c1)–(c5) Exp-hyb0.3, and for the 45-min forecasts initialized at 2000 UTC from (d1)–(d4) Exp-PureEnVar, (e1)–(e4) Exp-Adaptive, and (f1)–(f4) Exp-NoAdaptive. The three observed supercells are labeled as A, B, and C in a north–south direction in (o1). The purple outline in (a1) is as in Fig. 13h but valid at 1945 UTC. The black contours in (e1) indicate the locations of applying the static BECs.

TABLE 5. List of the single cycle DA experiments to reveal the impact of the adaptive hybridization. The analysis time is valid at 2000 UTC 20 May 2013. The same first-guess and ensemble from Exp-PureEnVar in Table 3 are used in three experiments. To demonstrate the effect of the static BECs in hybrid EnVar, the full BECs in Exp-Adaptive and Exp-NoAdaptive comprise 0.7/0.3 weights between static and ensemble covariances.

Expt	Configurations
Exp-PureEnVar	Same as Exp-PureEnVar in Table 3, using full ensemble covariances
Exp-Adaptive	Adaptively incorporating the static BECs
Exp-NoAdaptive	Applying the static BECs to the entire domain

BECs in hybrid EnVar when the ensemble covariance shows deficiencies.

This study introduces an approach to construct the convective-scale static BEC matrix for direct radar reflectivity assimilation. As an initial effort to illustrate the approach, the demonstrations for the approach are only obtained from one isolated tornadic supercell event and one multisupercell event. Systematic experiments using more cases are warranted for future studies. In addition to the storm intensity-dependent binning method, given that different climatological background-error statistics may exist among various convection and storm types (e.g., isolated supercells versus organized mesoscale convective systems), efforts toward constructing static BECs and simultaneously implementing them for a variety of convective-scale scenarios concurrently occurring over the CONUS may likely be needed. Moreover, although the adaptive hybridization performs as expected for the two cases examined, further examination is required for the multiple convective-scale scenarios over the CONUS. As discussed earlier, one application of the constructed convective-scale static covariance is to directly improve 3DVar, 4DVar, and hybrid EnVar for convective-scale analysis and prediction. Static covariance can also be used to mitigate the ensemble deficiency in a pure EnKF through sampling and adding coherent perturbations to the storm areas (Wang et al. 2009). This study investigates the impact of static BECs in hybrid EnVar when the RTPS is used to inflate the ensemble. Additional study of the impact of the static covariance when other approaches are used to improve the sampling of the ensemble such as stochastic physics (Gasperoni et al. 2020) and additive perturbation approach (Dowell and Wicker 2009) is left for future studies.

Acknowledgments. This study was primarily supported by NA16OAR4590236, NA16OAR4320115, NA16OAR3420115, and NA19OAR4590231. The computation in this study was conducted at the University of Oklahoma Supercomputing Center for Education and Research (OSCER). Nicholas A. Gasperoni and Yue Yang are acknowledged for helping to proofread the manuscript. Finally, we thank three anonymous reviewers for their very helpful comments that substantially improved the quality of this manuscript.

REFERENCES

Albers, S. C., J. A. McGinley, D. L. Birkenheuer, and J. R. Smart, 1996: The Local Analysis and Prediction System (LAPS): Analyses of clouds, precipitation, and temperature. *Wea. Forecasting*, **11**, 273–287, https://doi.org/10.1175/1520-0434(1996)011<0273:TLAAPS>2.0.CO;2.

Barker, D. M., and Coauthors, 2004: A three-dimensional variational data assimilation system for MM5: Implementation and initial results. *Mon. Wea. Rev.*, **132**, 897–914, https://doi.org/10.1175/1520-0493(2004)132<0897:ATVDAS>2.0.CO;2.

Berre, L., 2000: Estimation of synoptic and mesoscale forecast error covariances in a limited-area model. *Mon. Wea. Rev.*, **128**, 644–667, https://doi.org/10.1175/1520-0493(2000)128<0644:EOSAMF>2.0.CO;2.

Brousseau, P., and Coauthors, 2008: A prototype convective-scale data assimilation system for operation: The AROME-RUC. HIRLAM Tech. Rep. 68, 8 pp.

Buehner, M., 2005: Ensemble-derived stationary and flow-dependent background-error covariances: Evaluation in a quasi-operational NWP setting. *Quart. J. Roy. Meteor. Soc.*, **131**, 1013–1043, https://doi.org/10.1256/qj.04.15.

——, P. L. Houtekamer, C. Charette, H. L. Mitchell, and B. He, 2010a: Intercomparison of variational data assimilation and the ensemble Kalman filter for global deterministic NWP. Part I: Description and single-observation experiments. *Mon. Wea. Rev.*, **138**, 1550–1566, https://doi.org/10.1175/2009MWR3157.1.

——, ——, ——, ——, and ——, 2010b: Intercomparison of variational data assimilation and the ensemble Kalman filter for global deterministic NWP. Part II: One-month experiments with real observations. *Mon. Wea. Rev.*, **138**, 1567–1586, https://doi.org/10.1175/2009MWR3158.1.

——, J. Morneau, and C. Charette, 2013: Four-dimensional ensemble-variational data assimilation for global deterministic weather prediction. *Nonlinear Processes Geophys.*, **20**, 669–682, https://doi.org/10.5194/npg-20-669-2013.

——, and Coauthors, 2015: Implementation of deterministic weather forecasting systems based on ensemble–variational data assimilation at environment Canada. Part I: The global system. *Mon. Wea. Rev.*, **143**, 2532–2559, https://doi.org/10.1175/MWR-D-14-00354.1.

Carley, J. R., 2012: Hybrid ensemble-3DVar radar data assimilation for the short-term prediction of convective storms. Ph.D. dissertation, Purdue University, 205 pp.

Caron, J.-F., and L. Fillion, 2010: An examination of background error correlations between mass and rotational wind over precipitation regions. *Mon. Wea. Rev.*, **138**, 563–578, https://doi.org/10.1175/2009MWR2998.1.

Caya, A., J. Sun, and C. Snyder, 2005: A comparison between the 4DVAR and the ensemble Kalman filter techniques for radar data assimilation. *Mon. Wea. Rev.*, **133**, 3081–3094, https://doi.org/10.1175/MWR3021.1.

Chen, F., and J. Dudhia, 2001: Coupling an advanced land surface–hydrology model with the Penn State–NCAR MM5 modeling system. Part I: Model implementation and sensitivity. *Mon. Wea. Rev.*, **129**, 569–585, https://doi.org/10.1175/1520-0493(2001)129<0569:CAALSH>2.0.CO;2.

Clark, A. J., and Coauthors, 2020: A real-time, simulated forecasting experiment for advancing the prediction of hazardous convective weather. *Bull. Amer. Meteor. Soc.*, **101**, E2022–E2024, https://doi.org/10.1175/BAMS-D-19-0298.1.

Clayton, A. M., A. C. Lorenc, and D. M. Barker, 2013: Operational implementation of a hybrid ensemble/4D-Var global data assimilation system at the Met Office. *Quart. J. Roy. Meteor. Soc.*, **139**, 1445–1461, https://doi.org/10.1002/qj.2054.

Daley, R., 1991: *Atmospheric Data Analysis*. Cambridge University Press, 457 pp.

Dee, D. P., and A. M. Da Silva, 2003: The choice of variable for atmospheric moisture analysis. *Mon. Wea. Rev.*, **131**, 155–171, https://doi.org/10.1175/1520-0493(2003)131<0155:TCOVFA>2.0.CO;2.

Derber, J., and A. Rosati, 1989: A global oceanic data assimilation system. *J. Phys. Oceanogr.*, **19**, 1333–1347, https://doi.org/10.1175/1520-0485(1989)019<1333:AGODAS>2.0.CO;2.

——, and F. Bouttier, 1999: A reformulation of the background error covariance in the ECMWF global data assimilation system. *Tellus*, **51A**, 195–221, https://doi.org/10.3402/tellusa.v51i2.12316.

Descombes, G., T. Auligné, F. Vandenberghe, D. M. Barker, and J. Barré, 2015: Generalized background error covariance matrix model (GEN-BE v2.0). *Geosci. Model Dev.*, **8**, 669–696, https://doi.org/10.5194/gmd-8-669-2015.

Dowell, D. C., and L. J. Wicker, 2009: Additive noise for storm-scale ensemble data assimilation. *J. Atmos. Oceanic Technol.*, **26**, 911–927, https://doi.org/10.1175/2008JTECHA1156.1.

——, F. Zhang, L. J. Wicker, C. Snyder, and N. A. Crook, 2004: Wind and temperature retrievals in the 17 May 1981 Arcadia, Oklahoma, supercell: Ensemble Kalman filter experiments. *Mon. Wea. Rev.*, **132**, 1982–2005, https://doi.org/10.1175/1520-0493(2004)132<1982:WATRIT>2.0.CO;2.

——, L. J. Wicker, C. Snyder, D. C. Dowell, L. J. Wicker, and C. Snyder, 2011: Ensemble Kalman filter assimilation of radar observations of the 8 May 2003 Oklahoma City supercell: Influences of reflectivity observations on storm-scale analyses. *Mon. Wea. Rev.*, **139**, 272–294, https://doi.org/10.1175/2010MWR3438.1.

Duda, J. D., X. Wang, Y. Wang, J. R. Carley, 2019: Comparing the assimilation of radar reflectivity using the direct GSI-based ensemble–variational (EnVar) and indirect cloud analysis methods in convection-allowing forecasts over the continental United States. *Mon. Wea. Rev.*, **147**, 1655–1678, https://doi.org/10.1175/MWR-D-18-0171.1.

Fisher, M., 2003: Background error covariance modeling. *Proc. ECMWF Seminar on Recent Developments in Data Assimilation for Atmosphere and Ocean*, Reading, United Kingdom, ECMWF, 45–64.

Gao, J., and D. J. Stensrud, 2012: Assimilation of reflectivity data in a convective-scale, cycled 3DVAR framework with hydrometeor classification. *J. Atmos. Sci.*, **69**, 1054–1065, https://doi.org/10.1175/JAS-D-11-0162.1.

——, and ——, 2014: Some observing system simulation experiments with a hybrid 3DEnVAR system for storm-scale radar data assimilation. *Mon. Wea. Rev.*, **142**, 3326–3346, https://doi.org/10.1175/MWR-D-14-00025.1.

——, M. Xue, A. Shapiro, and K. K. Droegemeier, 1999: A variational method for the analysis of three-dimensional wind fields from two Doppler radars. *Mon. Wea. Rev.*, **127**, 2128–2142, https://doi.org/10.1175/1520-0493(1999)127<2128:AVMFTA>2.0.CO;2.

——, ——, K. Brewster, and K. K. Droegemeier, 2004: A three-dimensional variational data analysis method with recursive filter for Doppler radars. *J. Atmos. Oceanic Technol.*, **21**, 457–469, https://doi.org/10.1175/1520-0426(2004)021<0457:ATVDAM>2.0.CO;2.

——, ——, and D. J. Stensrud, 2013: The development of a hybrid EnKF-3DVAR algorithm for storm-scale data assimilation. *Adv. Meteor.*, **2013**, 512–656, https://doi.org/10.1155/2013/512656.

Gasperoni, N. A., X. Wang, and Y. Wang, 2020: A comparison of methods to sample model errors for convection-allowing ensemble forecasts in the setting of multiscale initial conditions produced by the GSI-based EnVar assimilation system. *Mon. Wea. Rev.*, **148**, 1177–1203, https://doi.org/10.1175/MWR-D-19-0124.1.

Hayden, C. M., and R. J. Purser, 1995: Recursive filter objective analysis of meteorological fields: Applications to NESDIS operational processing. *J. Appl. Meteor.*, **34**, 3–15, https://doi.org/10.1175/1520-0450-34.1.3.

Hu, M., and M. Xue, 2007: Impact of configurations of rapid intermittent assimilation of WSR-88D radar data for the 8 May 2003 Oklahoma City tornadic thunderstorm case. *Mon. Wea. Rev.*, **135**, 507–525, https://doi.org/10.1175/MWR3313.1.

——, ——, and K. Brewster, 2006: 3DVAR and cloud analysis with WSR-88D level-II data for the prediction of the Fort Worth, Texas, tornadic thunderstorms. Part I: Cloud analysis and its impact. *Mon. Wea. Rev.*, **134**, 675–698, https://doi.org/10.1175/MWR3092.1.

Huang, X.-Y., and Coauthors, 2009: Four-dimensional variational data assimilation for WRF: Formulation and preliminary results. *Mon. Wea. Rev.*, **137**, 299–314, https://doi.org/10.1175/2008MWR2577.1.

Iacono, M. J., J. S. Delamere, E. J. Mlawer, M. W. Shephard, S. A. Clough, and W. D. Collins, 2008: Radiative forcing by long-lived greenhouse gases: Calculations with the AER radiative transfer models. *J. Geophys. Res.*, **113**, D13103, https://doi.org/10.1029/2008JD009944.

Ingleby, N., 2001: The statistical structure of forecast errors and its representation in The Met. Office global 3-D variational data assimilation scheme. *Quart. J. Roy. Meteor. Soc.*, **127**, 209–231, https://doi.org/10.1002/qj.49712757112.

Janjić, Z. I., 1990: The step-mountain coordinate: Physical package. *Mon. Wea. Rev.*, **118**, 1429–1443, https://doi.org/10.1175/1520-0493(1990)118<1429:TSMCPP>2.0.CO;2.

——, 1994: The step-mountain eta coordinate model: Further developments of the convection, viscous sublayer, and turbulence closure schemes. *Mon. Wea. Rev.*, **122**, 927–945, https://doi.org/10.1175/1520-0493(1994)122<0927:TSMECM>2.0.CO;2.

——, 2002: Nonsingular implementation of the Mellor–Yamada level 2.5 scheme in the NCEP Meso Model. NCEP Office Note 437, 61 pp.

Johnson, A., and Coauthors, 2015: A comparison of multiscale GSI-based EnKF and 3DVar data assimilation using radar and conventional observations for midlatitude convective-scale precipitation forecasts. *Mon. Wea. Rev.*, **143**, 3087–3108, https://doi.org/10.1175/MWR-D-14-00345.1.

Kong, R., M. Xue, and C. Liu, 2018: Development of a hybrid En3DVar data assimilation system and comparisons with 3DVar and EnKF for radar data assimilation with observing system simulation experiments. *Mon. Wea. Rev.*, **146**, 175–198, https://doi.org/10.1175/MWR-D-17-0164.1.

Lakshmanan, V., T. Smith, G. Stumpf, and K. Hondl, 2007: The Warning Decision Support System–Integrated Information. *Wea. Forecasting*, **22**, 596–612, https://doi.org/10.1175/WAF1009.1.

Li, Y., X. Wang, and M. Xue, 2012: Assimilation of radar radial velocity data with the WRF hybrid ensemble–3DVAR system for the prediction of Hurricane Ike (2008). *Mon. Wea. Rev.*, **140**, 3507–3524, https://doi.org/10.1175/MWR-D-12-00043.1.

Lilly, D. K., 1990: Numerical prediction of thunderstorms—Has its time come? *Quart. J. Roy. Meteor. Soc.*, **116**, 779–798.

Liu, C. S., M. Xue, and R. Kong, 2019: Direct assimilation of radar reflectivity data using 3DVAR: Treatment of hydrometeor background errors and OSSE tests. *Mon. Wea. Rev.*, **147**, 17–29, https://doi.org/10.1175/MWR-D-18-0033.1.

Lorenc, A. C., and Coauthors, 2000: The Met.Office global three-dimensional variational data assimilation scheme. *Quart. J. Roy. Meteor. Soc.*, **126**, 2991–3012, https://doi.org/10.1002/qj.49712657002.

Mellor, G. L., and T. Yamada, 1982: Development of a turbulence closure model for geophysical fluid problems. *Rev. Geophys. Space Phys.*, **20**, 851–875, https://doi.org/10.1029/RG020i004p00851.

Ménétrier, B., and T. Montmerle, 2011: Heterogeneous background-error covariances for the analysis and forecast of fog events. *Quart. J. Roy. Meteor. Soc.*, **137**, 2004–2013, https://doi.org/10.1002/qj.802.

Michel, Y., T. Auligné, and T. Montmerle, 2011: Heterogeneous convective-scale background error covariances with the inclusion of hydrometeor variables. *Mon. Wea. Rev.*, **139**, 2994–3015, https://doi.org/10.1175/2011MWR3632.1.

Minamide, M., and F. Zhang, 2019: An adaptive background error inflation method for assimilating all-sky radiances. *Quart. J. Roy. Meteor. Soc.*, **145**, 805–823, https://doi.org/10.1002/qj.3466.

Montmerle, T., and L. Berre, 2010: Diagnosis and formulation of heterogeneous background-error covariances at the mesoscale. *Quart. J. Roy. Meteor. Soc.*, **136**, 1408–1420, https://doi.org/10.1002/qj.655.

——, Y. Michel, E. Arbogast, B. Ménétrier, and P. Brousseau, 2018: A 3D ensemble variational data assimilation scheme for the limited-area AROME model: Formulation and preliminary results. *Quart. J. Roy. Meteor. Soc.*, **144**, 2196–2215, https://doi.org/10.1002/qj.3334.

Purser, R. J., W.-S. Wu, D. F. Parrish, and N. M. Roberts, 2003a: Numerical aspects of the application of recursive filters to variational statistical analysis. Part I: Spatially homogeneous and isotropic Gaussian covariances. *Mon. Wea. Rev.*, **131**, 1524–1535, https://doi.org/10.1175//1520-0493(2003)131<1524:NAOTAO>2.0.CO;2.

——, ——, ——, and ——, 2003b: Numerical aspects of the application of recursive filters to variational statistical analysis. Part II: Spatially inhomogeneous and anisotropic general covariances. *Mon. Wea. Rev.*, **131**, 1536–1548, https://doi.org/10.1175//2543.1.

Romine, G. S., D. W. Burgess, and R. B. Wilhelmson, 2008: A dual-polarization-radar-based assessment of the 8 May 2003 Oklahoma City area tornadic supercell. *Mon. Wea. Rev.*, **136**, 2849–2870, https://doi.org/10.1175/2008MWR2330.1.

Schwartz, C. S., 2016: Improving large-domain convection-allowing forecasts with high-resolution analyses and ensemble data assimilation. *Mon. Wea. Rev.*, **144**, 1777–1803, https://doi.org/10.1175/MWR-D-15-0286.1.

Sun, J., 2005: Convective-scale assimilation of radar data: Progress and challenges. *Quart. J. Roy. Meteor. Soc.*, **131**, 3439–3463, https://doi.org/10.1256/qj.05.149.

——, and N. A. Crook, 1997: Dynamical and microphysical retrieval from Doppler radar observations using a cloud model and its adjoint. Part I: Model development and simulated data experiments. *J. Atmos. Sci.*, **54**, 1642–1661, https://doi.org/10.1175/1520-0469(1997)054<1642:DAMRFD>2.0.CO;2.

——, D. W. Flicker, and D. K. Lilly, 1991: Recovery of three-dimensional wind and temperature fields from single-Doppler radar data. *J. Atmos. Sci.*, **48**, 876–890, https://doi.org/10.1175/1520-0469(1991)048<0876:ROTDWA>2.0.CO;2.

——, H. Wang, W. Tong, Y. Zhang, C.-Y. Lin, and D. Xu, 2016: Comparison of the impacts of momentum control variables on high-resolution variational data assimilation and precipitation forecasting. *Mon. Wea. Rev.*, **144**, 149–169, https://doi.org/10.1175/MWR-D-14-00205.1.

Thompson, G., P. R. Field, R. M. Rasmussen, and W. R. Hall, 2008: Explicit forecasts of winter precipitation using an improved bulk microphysics scheme. Part II: Implementation of a new snow parameterization. *Mon. Wea. Rev.*, **136**, 5095–5115, https://doi.org/10.1175/2008MWR2387.1.

Wang, H., J. Sun, S. Fan, and X.-Y. Huang, 2013a: Indirect assimilation of radar reflectivity with WRF 3D-Var and its impact on prediction of four summertime convective events. *J. Appl. Meteor. Climatol.*, **52**, 889–902, https://doi.org/10.1175/JAMC-D-12-0120.1.

——, ——, X. Zhang, X. Huang, and T. Auligne, 2013b: Radar data assimilation with WRF 4D-Var. Part I: System development and preliminary testing. *Mon. Wea. Rev.*, **141**, 2224–2244, https://doi.org/10.1175/MWR-D-12-00168.1.

Wang, X., 2010: Incorporating ensemble covariance in the gridpoint statistical interpolation variational minimization: A mathematical framework. *Mon. Wea. Rev.*, **138**, 2990–2995, https://doi.org/10.1175/2010MWR3245.1.

——, T. M. Hamill, J. S. Whitaker, and C. H. Bishop, 2007a: A comparison of hybrid ensemble transform Kalman filter-optimum interpolation and ensemble square root filter analysis schemes. *Mon. Wea. Rev.*, **135**, 1055–1076, https://doi.org/10.1175/MWR3307.1.

——, C. Snyder, and T. M. Hamill, 2007b: On the theoretical equivalence of differently proposed ensemble–3DVAR hybrid analysis schemes. *Mon. Wea. Rev.*, **135**, 222–227, https://doi.org/10.1175/MWR3282.1.

——, D. M. Barker, C. Snyder, T. M. Hamill, X. Wang, D. M. Barker, C. Snyder, and T. M. Hamill, 2008a: A hybrid ETKF–3DVAR data assimilation scheme for the WRF Model. Part I: Observing system simulation experiment. *Mon. Wea. Rev.*, **136**, 5116–5131, https://doi.org/10.1175/2008MWR2444.1.

——, ——, ——, and ——, 2008b: A hybrid ETKF–3DVAR data assimilation scheme for the WRF Model. Part II: Real observation experiments. *Mon. Wea. Rev.*, **136**, 5132–5147, https://doi.org/10.1175/2008MWR2445.1.

——, T. M. Hamill, J. S. Whitaker, and C. H. Bishop, 2009: A comparison of the hybrid and EnSRF analysis schemes in the presence of model error due to unresolved scales. *Mon. Wea. Rev.*, **137**, 3219–3232, https://doi.org/10.1175/2009MWR2923.1.

——, D. Parrish, D. Kleist, and J. S. Whitaker, 2013: GSI 3DVar-based ensemble-variational hybrid data assimilation for NCEP global forecast system: Single resolution experiments. *Mon. Wea. Rev.*, **141**, 4098–4117, https://doi.org/10.1175/MWR-D-12-00141.1.

Wang, Y., and X. Wang, 2017: Direct assimilation of radar reflectivity without tangent linear and adjoint of the nonlinear observation operator in the GSI-based EnVar system: Methodology and experiment with the 8 May 2003 Oklahoma City tornadic supercell. *Mon. Wea. Rev.*, **145**, 1447–1471, https://doi.org/10.1175/MWR-D-16-0231.1.

——, and ——, 2020: Prediction of tornado-like vortex (TLV) embedded in the 8 May 2003 Oklahoma City tornadic supercell initialized from the subkilometer grid spacing analysis produced by the dual-resolution GSI-based EnVar data assimilation system. *Mon. Wea. Rev.*, **148**, 2909–2934, https://doi.org/10.1175/MWR-D-19-0179.1.

Wang, Y.-H., J. Gao, P. S. Skinner, K. Knopfmeier, T. Jones, G. Creager, P. L. Heiselman, and L. J. Wicker, 2019: Test of a weather-adaptive dual-resolution hybrid warn-on-forecast analysis and forecast system for several severe weather events. *Wea. Forecasting*, **34**, 1807–1827, https://doi.org/10.1175/WAF-D-19-0071.1.

Whitaker, J. S., and T. M. Hamill, 2002: Ensemble data assimilation without perturbed observations. *Mon. Wea. Rev.*, **130**,

1913–1924, https://doi.org/10.1175/1520-0493(2002)130<1913:EDAWPO>2.0.CO;2.

——, and ——, 2012: Evaluating methods to account for system errors in ensemble data assimilation. *Mon. Wea. Rev.*, **140**, 3078–3089, https://doi.org/10.1175/MWR-D-11-00276.1.

Wu, W., and J. Purser, 2002: Three-dimensional variational analysis with spatially inhomogeneous covariances. *Mon. Wea. Rev.*, **130**, 2905–2916, https://doi.org/10.1175/1520-0493(2002)130<2905:TDVAWS>2.0.CO;2.

Xiao, Q., Y.-H. Kuo, J. Sun, W.-C. Lee, E. Lim, Y. Guo, and D. M. Barker, 2005: Assimilation of Doppler radar observations with a regional 3D-Var system: Impact of Doppler velocities on forecasts of a heavy rainfall case. *J. Appl. Meteor.*, **44**, 768–788, https://doi.org/10.1175/JAM2248.1.

Xie, Y., and A. E. MacDonald, 2012: Selection of momentum variables for a three-dimensional variational analysis. *Pure Appl. Geophys.*, **169**, 335–351, https://doi.org/10.1007/s00024-011-0374-3.

Yussouf, N., E. R. Mansell, L. J. Wicker, D. M. Wheatley, and D. J. Stensrud, 2013: The ensemble Kalman filter analyses and forecasts of the 8 May 2003 Oklahoma City tornadic supercell storm using single- and double-moment microphysics schemes. *Mon. Wea. Rev.*, **141**, 3388–3412, https://doi.org/10.1175/MWR-D-12-00237.1.

Zou, X., Y.-H. Kuo, and Y.-R. Guo, 1995: Assimilation of atmospheric radio refractivity using a nonhydrostatic adjoint model. *Mon. Wea. Rev.*, **123**, 2229–2249, https://doi.org/10.1175/1520-0493(1995)123<2229:AOARRU>2.0.CO;2.